Global-scale evaluation of coastal ocean alkalinity enhancement in a fully-coupled Earth system model

Julien Palmiéri[1,2], **Andrew Yool**[1,2]

[1]National Oceanography Centre, European Way, Southampton, SO14 3ZH, UK
[2]These authors contributed equally to the work

Key Points:

- Coastal ocean alkalinity enhancement scheme investigated using state-of-the-art Earth system model with fully-coupled carbon cycle
- Overall air-sea CO_2 uptake enhanced 8% under high emissions scenario, and atmospheric xCO_2 declines by 10 ppm
- Almost 50% of additional CO_2 uptake takes place away from OAE locations with implications for measurement, reporting and verification

Corresponding author: Andrew Yool, axy@noc.ac.uk

Abstract

The Paris Climate Accords plan for "net-zero" carbon dioxide (CO_2) by 2050. However, reducing emissions from some sectors is challenging, and "net-zero" permits carbon dioxide removal (CDR) activities. One CDR scheme is ocean alkalinity enhancement (OAE), which proposes to dissolve basic minerals into seawater to increase its total alkalinity (TA) and buffering capacity for CO_2. While modelling studies have often investigated OAE by adding TA to the ocean's surface at basin or global scale, some proposals focus on readily-accessible coastal shelves, with TA added through the dissolution of olivine sands. Critically, by settling and dissolving sands on shallow seafloors, this retains the added TA in near-surface waters in direct contact with atmospheric CO_2. To investigate this, we add dissolved TA to the global shelves (¡100m) of an Earth system model (UKESM1) running a high emissions scenario. As UKESM1 is fully-coupled, wider effects of OAE-mediated increase in ocean CO_2 uptake –e.g. atmospheric xCO_2, air temperature and marine pH– are fully-quantified. Applying OAE from 2020-2100 decreases atmospheric xCO_2 ∼10 ppm, and increases air-to-sea CO_2 uptake ∼8%. Due to advection of added TA, ∼50% of this uptake occurs remotely from OAE operations. In-line with other studies, CO_2 uptake per unit of TA added occurs at a rate of ∼0.8 mol C (mol TA)$^{-1}$, though this is elevated in enclosed regions. Meanwhile, changes in air temperature and marine pH are indistinguishable from natural variability. While practical uncertainties and model representation caveats remain, this analysis estimates the effectiveness of this specific OAE scheme to assist with net-zero planning.

Plain Language Summary

The Paris Agreement aims to limit climate warming to 1.5°C by achieving net-zero carbon dioxide (CO_2) emissions by 2050. As it is difficult to abate all CO_2 emissions for some sectors of human activity, carbon dioxide removal (CDR) schemes will be needed to offset residual emissions. One of these is ocean alkalinity enhancement (OAE), which proposes elevating the ocean's storage capacity for CO_2 by increasing its alkalinity through the addition of basic minerals as solutions or particulates. The latter require time to dissolve but risk sinking away from the ocean's surface where they absorb CO_2. Coastal OAE proposes adding particulate minerals on the shallow continental shelves, where dissolution products will remain within the upper water column. Here we examine coastal OAE inside a state-of-the-art Earth system model to quantify its CO_2 uptake, where this occurs, its efficiency (carbon stored per unit alkalinity added), and its impacts on atmospheric CO_2 concentration and climate. Overall, coastal OAE enhanced CO_2 uptake, and did so with an efficiency of almost 0.8, but even with global deployment, atmospheric and climate changes are small. Furthermore, almost 50% of the additional CO_2 uptake took place away OAE operations, indicating challenges for monitoring the effectiveness of real-world deployment.

1 Introduction

The climate of the Earth system (ES) is undergoing rapid change with an increase in global mean surface air temperature (SAT) by 1.09°C between the periods 1850-1900 and 2011-2020. This is largely due to anthropogenic emissions of the greenhouse gas carbon dioxide (CO_2) that have increased its atmospheric concentration from approximately 278 parts per million (ppm) prior to the Industrial Revolution (∼1750) to 417.05 ppm as of 2022 (Lan et al., 2023). The Paris Agreement (PA), currently adopted by 194 UN member states, was drafted in 2015 with the aim of limiting climate warming to well below the threshold of temperature 2°C, and ideally below a target of 1.5°C (Schellnhuber et al., 2016). A key element in the framing of the PA is the rapid reduction in these CO_2 emissions, with the aim to reach so-called "net zero" emissions by 2050, at which point any remaining CO_2 emissions should be balanced by active measures that remove it from

the atmosphere (Rogelj et al., 2018). These measures should effectively provide "negative emissions" that operate in addition to natural terrestrial and oceanic processes to draw down atmospheric CO_2 to end climate warming. However, achieving this requires the deployment of proven carbon dioxide removal (CDR) technologies at a scale that is sufficient to counter residual emissions (Williamson, 2016).

These technologies span a range from first-order ones such as direct air capture (DAC) that remove CO_2 from the atmosphere (e.g. Mahmoudkhani & Keith, 2009; Sanz-Pérez et al., 2016), through to those involving modification of terrestrial and marine components of the ES, and may involve their associated living systems (Hartmann et al., 2013). Examples from on the terrestrial side include enhanced or restored natural vegetation stocks (e.g. forests), the production and surface burial of long-lived biochar from terrestrial biomass, and the use of terrestrial biomass in conjunction with carbon capture and storage (BECCS; Lenton, 2010). On the marine side, examples include the restoration of marine vegetation stocks (e.g. kelp, seagrasses; Shayka et al., 2023) especially where associated with sedimentation and burial, and the fertilisation of plankton ecosystems either by direct nutrient addition (e.g. iron fertilisation; Lampitt et al., 2008) or enhanced nutrient upwelling (e.g. ocean pipes; Yool et al., 2009). However, a further proposed marine technology, ocean alkalinity enhancement (OAE), instead focuses on the modification of seawater chemistry to enhance the capacity of the ocean to uptake and store CO_2 from the atmosphere (Kheshgi, 1995).

In the natural background state of the ES, the ocean is the largest active reservoir of CO_2, with more than 92% of the total stored as dissolved inorganic carbon (DIC; Raven & Falkowski, 1999). While augmented by marine biology, this dominance of the ocean stems from the solubility of CO_2 in seawater, and its reaction with water into bicarbonate (HCO_3^-) and carbonate (CO_3^{2-}) ions that do not directly interact with the atmosphere. The balance of these three carbon species (DIC = $CO_2(aq)$ + HCO_3^- + CO_3^{2-}) is a function of ambient temperature, salinity and the quantity known as total alkalinity (TA) that effectively buffers this balance. In general terms, higher seawater TA tips the balance of DIC towards HCO_3^- and CO_3^{2-} ions, and allows seawater to store greater concentrations of DIC. OAE proposes to modify seawater chemistry at scale to increase alkalinity and to favour the solubility of CO_2, removing it from the atmosphere to solution in the ocean.

Originally proposed by Kheshgi (1995), OAE is also referred to as "enhanced weathering" (EW) in reference to its mimicking of the natural weathering of typically silicate rocks that modulates ocean TA on geological timescales (Renforth, 2012). As presently envisaged, OAE involves increasing surface seawater TA to enhance its buffering capacity for CO_2, typically through the dissolution of large quantities of naturally-occurring silicate or carbonate minerals. The source of suitable minerals potentially includes mineral derivatives that may conventionally be viewed as "waste products" from unrelated industrial activities (Bullock et al., 2022). It is critical for this dissolution to occur in near-surface waters in order that the TA added is exposed to atmospheric CO_2, and so the processing, grinding, delivery and dissolution dynamics of minerals are important considerations. A separate approach to OAE is the electrochemical production and distribution of dissolved sodium hydroxide (NaOH) directly into the ocean, and this would avoid the dissolution timescales and sinking away from the surface associated with particulate minerals. Note that, though we focus here on OAE, the use of EW has largely focused on terrestrial applications, for instance where mined minerals are distributed over the land surface to weather (and absorb CO_2) at an enhanced rate (e.g. Renforth, 2012).

Currently, a number of field trials of OAE are being undertaken internationally, both by academic researchers (e.g. Albright et al., 2016; Voosen, 2022) and by private companies (e.g. Tollesfon, 2023). These trials have involved the use of different sources of TA, including sodium hydroxide (Albright et al., 2016), powdered lime (Voosen, 2022), and olivine sands (Tollesfon, 2023). And they have examined a range of different impacts

of the OAE application including changes in local carbonate chemistry, redistribution of the applied minerals, enhancement of seawater CO_2, and the impacts of heavy metal contaminants released as certain alkaline minerals dissolve. While these trials have been relatively small scale to date, they have generally found positive results that are supportive of OAE in principle, although not without complications (e.g. potential burial of olivine sands instead of dissolution; Tollesfon, 2023). Separately, controlled laboratory studies have investigated the risk of runaway calcium carbonate ($CaCO_3$) precipitation potentially caused by the excursions in local carbonate chemistry triggered by OAE (Moras et al., 2022; Hartmann et al., 2023). Such $CaCO_3$ precipitation is an important practical consideration for OAE since, were it to occur, it would effectively remove the added TA from seawater, preventing it from absorbing CO_2 from the atmosphere. These studies have determined ranges of local environmental conditions (temperature, colloidal material) and TA perturbations that permit effective OAE operations.

The wider effectiveness of OAE has also been evaluated using models run from local to regional to global scales. The first assessment of OAE at global scale was the pioneering study of Ilyina et al. (2013), which used an ocean-only model to investigate OAE applications at both full-global and regional scales. This study linked TA additions to CO_2 emissions for a range of fixed ratios, and found that it was possible to maintain ocean properties such as pH at present-day values, but that the scale of OAE required dwarfed addition of TA through natural geological weathering. The subsequent study of Feng et al. (2017) used an Earth system model of Intermediate Complexity (EMIC), and while also global, applied OAE solely in coastal regions after explicitly calculating the dissolution rate from grain size and ambient temperature and pH. This study explored relatively high rates of OAE that, under the best conditions examined, almost halved atmospheric CO_2 concentrations (xCO_2), and it found that grain size a critical factor in particle dissolution rates. More recently, He and Tyka (2023) investigated spatio-temporal aspects of OAE in ocean-only simulations with point versus distributed TA addition, and with continuous versus pulsed additions. This work found OAE efficiency plateaued after 3-4 years, and that OAE near deep-water formation areas had reduced efficiency (e.g. Iceland). While these groundbreaking studies focused at global scale, a number of studies have explored more localised situations. Feng et al. (2016) investigated the potential for regional OAE to assist with preserving tropical coral reef ecosystems, generally finding that it could prevent carbonate chemistry measures from crossing critical thresholds. Meanwhile, Butenschön et al. (2021) focused on high-resolution modelling of OAE in the Mediterranean Sea, while Wang and Dreisinger (2022) focused on point releases in the Bering Sea. The increasing role of large-scale modelling to investigate OAE led to the initiation of the Carbon Dioxide Removal Model Intercomparison Project (CDRMIP) to provide a common protocol for idealised global-scale OAE to be investigated in a series of standardised experiments (Keller et al., 2018). CDRMIP was instigated during the sixth phase of the Coupled Model Intercomparison Project (CMIP6), and aims to entrain multiple Earth system models (ESMs) so that uncertainties, particularly those in marine physics and biogeochemistry, can be better understood.

In the investigation here, we parameterise a global-scale coastal OAE scheme with realistic TA addition within a state-of-the-art ESM and use this to simulate the operation of this scheme across the 21st century under a high emissions scenario. In using a global ESM with dynamic, fully-coupled atmosphere, ocean, land and biotic components, this study builds on previous work that has used lower complexity ocean-only models and EMICs, and those simulating limited regional domains. Primary evaluation of the potential impact of this scheme considers any additional ocean CO_2 uptake it drives, and the changes in atmospheric xCO_2 and SAT that result. Analysis also considers the TA added to the ocean together with the associated additional DIC, focusing on redistribution away from coastal regions and the "efficiency" with which extra DIC enters the ocean. Sensitivity analyses examine uncertainties in the dissolution rate of OAE minerals and the significance of the model's low vertical resolution.

2 Methods

2.1 Model description

The investigation here makes use of the UK Earth system model version 1.0 (henceforth UKESM1; Sellar et al., 2019). This model simulates the coupled physical–biogeochemical dynamics of the ocean, atmosphere and land components of the Earth, including their living components. The core physical climate model of UKESM1 is the Hadley Centre Global Environmental Model version 3 Global Coupled version 3.1 (HadGEM3-GC3.1; Williams et al., 2018; Kuhlbrodt et al., 2018). This core is expanded in UKESM1 by the inclusion of stratospheric-tropospheric trace gas chemistry, ocean biogeochemistry, and terrestrial ecology and biogeochemistry. These additions to HadGEM3-GC3.1 introduce extra cross-component couplings that may affect climate by adding feedback processes or new interactions – such as the sinks/sources of climate-relevant gases. UKESM1 participated in the Coupled Model Intercomparison Project (CMIP6; Eyring et al., 2016), and a full description of its specific model components can be found in Sellar et al. (2019) (and references therein).

The ocean component of UKESM1 is represented physically by the Nucleus for European Modelling of the Ocean framework (NEMO v3.6_stable; Madec et al., 2017), and biogeochemically by the Model of Ecosystem Dynamics, nutrient Utilisation, Sequestration and Acidification (MEDUSA-2; Yool et al., 2013). NEMO is composed of an ocean general circulation model, Océan PArallélisé version 9 (OPA9; Madec et al., 1997; Madec & Team, 2008), coupled to a separate sea ice model, the Los Alamos Sea Ice Model version 5.1.2 (CICE; Rae et al., 2015). The NEMO domain within UKESM1 is at a horizontal resolution of approximately 1-degree, and uses a tripolar model grid that incorporates an equatorial band of enhanced zonal resolution. Vertical space in NEMO is resolved into 75 z-levels ranging in thickness from approximately 1 m at the surface to approximately 200 m at abyssal depths. MEDUSA is a dual size class nutrient, phytoplankton, zooplankton, detritus (NPZD) model that represents the biogeochemical cycles of nitrogen, silicon, iron, carbon, oxygen and alkalinity. The alkalinity cycle in MEDUSA is highly simplified and only represents the net production, export and vertical dissolution of calcium carbonate ($CaCO_3$) down the water column. Net $CaCO_3$ production is calculated as a function of the downward flux of fast-sinking detrital particles and ambient carbonate chemistry (specifically the ambient saturation state of calcite, $\Omega_{calcite}$), with its dissolution only occurring below the calcite compensation depth (CCD) or at the seafloor. Surface (and interior) carbonate chemistry in MEDUSA is represented using MOCSY 2.0 (Orr & Epitalon, 2015). A full description of MEDUSA and its alkalinity cycle can be found in Yool et al. (2013).

A comprehensive evaluation of the realism of NEMO–MEDUSA in UKESM1 can be found in Yool et al. (2021), with a broader evaluation of its Earth system components in Sellar et al. (2019).

2.2 Experiment design

Ocean alkalinity enhancement is introduced into UKESM1 through specifying an addition of the model's alkalinity tracer at locally-calculated rates in shallow water shelf regions at a depth of 100 m. The experiment design aims to simulate the addition of olivine sands into coastal waters, the settling of these onto the shallow seafloor, and their subsequent dissolution to alkalinity within seawater that, through mixing, is in close proximity to the ocean's surface and the atmosphere. Equation 1 shows the dissolution reaction of olivine (here, Mg-rich forsterite) to ionic magnesium, biocarbonate and silicic acid (Schuiling & Krijgsman, 2006).

$$Mg_2SiO_4 + 4\ CO_2 + 4\ H_2O \rightarrow 2\ Mg^{2+} + 4\ HCO_3^- + H_4SiO_4 \quad (1)$$

This dissolution of olivine leads to the release of 4 equivalents of TA (eq) per mol of olivine. Equation 1 also suggests that this should sequester 4 mol of CO_2 as HCO_3^- per mol of olivine (= 1 mol CO_2 per 1 eq TA), although the situation is more complex in reality as both seawater TA and DIC are increased by dissolution, and this instead represents an idealised maximum (Köhler et al., 2010). Using representative mean values of ocean and atmosphere quantities, a sequestration ratio of ≈ 0.8 mol CO_2 (eq TA)$^{-1}$ has been estimated (Renforth & Henderson, 2017; Tyka et al., 2022).

To provide an upper estimate for the potential of this mode of OAE, the experiment design "scales up" this addition process to continuous addition across the entire global ocean wherever seafloor depth is shallower than 100 m. The rate of alkalinity addition is described in Equation 2 and illustrated in Figure 1a. It uses a temperature-dependent formulation (Rimstidt et al., 2012) calculated assuming that a 1 cm-thick layer of 250 μm diameter olivine spherical grains is in contact with porewater at a pH of 7.2. This layer was considered to have a porosity of 0.50, typical of coastal sandy sediments (Yu et al., 1993).

$$f_{Alk} = (0.00009 \times T^3) - (0.0003 \times T^2) + (0.0268 \times T) + 0.1964 \quad (2)$$

Where T is temperature, in degrees Celsius, and f_{Alk} is the flux of alkalinity from the olivine sand, in eq m^{-2} y^{-1}. For alignment with alkalinity addition in waters shallower than 100 m, the ambient seawater temperature used in Equation 2 is taken from the UKESM1 vertical grid cell overlapping 100 m, or from the deepest cell where the water column is shallower than 100 m.

Input regions are identified by mapping the area of seafloor shallower than 100 m from the 5-minute Gridded Global Relief Dataset, ETOPO5 (National Geophysical Data Center, 1993), to UKESM1's low resolution ocean grid, eORCA1. The resulting fractional area of each ocean grid cell is then used as a scaling factor for the total quantity of alkalinity added to each water column. Effectively, this means that individual UKESM1 water columns receive a quantity of alkalinity that is in proportion to the amount of seafloor that is 100 m or shallower in the real world location, rather than an amount based on the model's low-resolution local water column depth. By default, the calculated alkalinity flux is added within the vertical grid cell of UKESM1's eORCA1 grid that encompasses the 100 m horizon. Where the model's local bathymetry is shallower than 100 m, the alkalinity is added to the deepest grid cell.

OAE alkalinity is added directly to the simulation's background alkalinity field so is indistinguishable from this, and is transported by physical processes (advection, mixing) and translocated by biogeochemical processes ($CaCO_3$ export and dissolution) identically.

Figure 1b presents a global map showing the geographical distribution of the simulated OAE across the model domain. Addition is widespread across major shelf regions including the Arctic, East China and North seas, with addition fluxes greatest in warm water shelf regions such as the Amazonian shelf and, especially, the Indonesian / Malaysian archipelago.

In the real world, the dissolution of olivine sands also introduces other important elements into seawater, including silicon and iron, both used by phytoplankton as nutrients for growth. To simplify the experimental design here, the addition of these nutrients has been omitted so that the analysis can focus on the direct effects of alkalinity addition.

Similarly to the other OAE studies cited here, the details of our methodology differ from the idealised OAE protocol described by CDRMIP (Keller et al., 2018). In the idealised CDRMIP experiment, *CDR-ocean-alk* (default simulation *esm-ssp585-ocn-alk*), alkalinity is added uniformly across the global ocean (with the exception of sea-ice areas) at a constant, globally-integrated rate of 140 Teq y^{-1}. As the simulated addition

here is coastal-only and calculated dynamically, it is less than this idealised total, around only 20% in the 2020s, although the experimental design permits this to increase with warming temperatures (26.5 Teq y^{-1} → 36.6 Teq y^{-1}; Table 2) . *CDR-ocean-alk* also differs in its use of purely surface alkalinity addition, and does not consider mineral dissolution.

2.3 Simulation description

Table 1 lists and describes the experiments and sensitivity analyses performed during this study. The descriptions include the rate and depth of alkalinity addition in the experimental simulations.

The main experiment simulation, EXP1, uses the alkalinity function given in Equation 2 with the addition occurring at 100 m or shallower as already described. This is paralleled by a control simulation, CTRL, which is essentially a continuation of an existing UKESM1 simulation (see below).

Two pairs of sensitivity simulations are performed in addition to the main experiment. In the first pair, EXP2 and EXP3, the rate of alkalinity addition is respectively halved and doubled. These aim to provide insight into uncertainties around the dissolution of olivine sands and the efficiency with which the added alkalinity increases CO_2 absorption into seawater. The second pair, EXP4 and EXP5, retain the default alkalinity function, but simply add the same quantity of TA at shallower (0 m) and deeper (down to 200 m) depth horizons. These aim to span the limitations on bathymetry and mixing imposed by the model's relatively low horizontal resolution and missing shelf processes (e.g. tides) by effectively representing end members where the added TA is mixed to the surface (since added alkalinity can only interact with CO_2 at the surface) efficiently (EXP4) or only weakly (EXP5).

All experiments were initialised at the beginning of year 2020 using the Earth system state of an existing UKESM1 simulation already in the forward projections period (2015–2100) of a ScenarioMIP experiment. The specific forward projection used here is the Shared Socioeconomic Pathway 5 ("fossil-fueled development") with a warming rate of 8.5 W m^{-2} by 2100 (SSP585; O'Neill et al., 2016). OAE was assumed to continue throughout the 21st century.

This original UKESM1 simulation, and all of the experiments performed here, operate in "emissions mode" in which atmospheric CO_2 concentration (xCO_2) is dynamically calculated rather than fixed to a prescribed or time-varying concentration. As well as being responsive to anthropogenic emissions, atmospheric xCO_2 in this mode is also conservatively altered by the exchange of CO_2 with its biogeochemical reservoirs in the ocean and land components. Thus, the simulated atmospheric history of xCO_2 – and the wider climate – responds to the evolution of the ocean and land carbon cycles, including those driven by OAE. Note that, prior to beginning SSP585, the source UKESM1 simulation was integrated across the full Historical period (1850–2014) with estimated actual anthropogenic CO_2 emissions, and then the beginning of the ScenarioMIP period (2015–2019) with projected emissions.

3 Results

The OAE perturbations applied in the experiments interact with the dynamics of the simulated Earth system leading to divergence from the control simulation in specific detail. This divergence can result in local situations that are initially unexpected given the experimental simulations. For instance, while all of the experimental simulations involve the *addition of TA* on top of the quantity in the control simulation, the simple (experiment - control) differences can be locally negative rather than the expected positive

due to minor differences in modelled circulation. To reduce the confounding effect of this, results described below make use of multi-annual averages except where noted (see Discussion for more detail).

Figure 2 shows a series of time series panels that illustrate key ocean and atmosphere properties across the period that the simulated OAE in operation. Each panel shows the control, CTRL, and primary experiment, EXP1, simulations, together with the OAE rate sensitivity simulations, EXP2 and EXP3. Complementing these figures, Table 2 presents global mean and integral statistics of main carbon cycle quantities and fluxes for the 2020s and 2090s across the CTRL and all EXP simulations.

Panel 2a shows the total addition of TA to the model domain by the simulated OAE from 2020 to 2100. In all three experiments shown, the rate of addition rises during the experiment in response to increasing surface ocean temperature. Essentially, the experimental simulations imply that, to balance the dissolution of the added olivine, the rate of OAE activity itself is increased from 2020 to 2100. In the case of EXP1, the rate of addition of TA increases from 26.6 Peq y^{-1} during the 2020s to 36.6 Peq y^{-1} (+37.6%) in the 2090s, with comparable increases for EXP2 (+37.1%) and EXP3 (+36.6%).

Panel 2b shows the corresponding change in global mean surface TA over the same period. Between the 2020s and 2090s, surface TA in EXP1 rises from 2323 to 2341 meq m^{-3} (+0.8%), with EXP2 and EXP3 showing rises (+0.4%, +1.4% respectively) that are broadly comparable with the TA added in these experiments. However, not all of this change is driven by OAE. Between the 2020s and 2090s, surface TA in the CTRL experiment also increases by +0.1%, in part due to the acidification-related decline in the production and export of biogenic calcium carbonate ($CaCO_3$) in MEDUSA (Yool et al., 2013).

Panels 2c to 2f show the corresponding changes in the carbon cycle of the ocean. Note that, unlike ocean alkalinity, the background state of the carbon cycle in the CTRL simulation is already changing over the 21st century as a result of increasing atmospheric CO_2 (and associated climate changes). Consequently, changes driven by OAE in the EXP simulations are occurring against a significantly moving backdrop.

In Panel 2c, the air-ocean uptake of the CTRL simulation increases throughout the 21st century until around 2080, after which it begins to decline. With a few exceptional years driven by interannual variability, EXP1's integrated CO_2 flux consistently exceeds that of the control simulation. By 2100, the integrated CO_2 fluxes of the CTRL and EXP1 simulations are 380.9 and 405.4 Pg C respectively (since their branch point in 2020), an increase of +6.4% for EXP1, with approximately proportional increases for EXP2 (+3.3%) and EXP3 (+12.4%).

These net positive CO_2 fluxes drive increases in both surface DIC concentrations (Panel 2d) and ocean DIC inventory (Panel 2e). Surface DIC in the CTRL simulation increases from 2378 mmol m^{-3} in the 2020s to 2211 mmol m^{-3} by the 2090s (+6.4%). EXP1 exceeds this, reaching 2225 mmol m^{-3} by the 2090s, an increase over the CTRL simulation at the same point of +0.6%. While ocean DIC inventory in Panel 2e shows a similar general pattern to surface concentration, the scale is much more modest because of the ocean's large background DIC inventory and relatively slow turnover. As indicated in Table 2, ocean DIC is increased by 0.06% in EXP1 over the CTRL simulation.

Finally, Panel 2f shows atmospheric CO_2 concentration (xCO_2). Again, the differences between the CTRL and EXP1 simulations appear modest because of the large changes that already occur during the SSP585 scenario, which sees atmospheric xCO_2 almost triple from around 400 in 2020 to around 1200 ppmv by 2100. Per Table 2, EXP1 exhibits a 2090s concentration -9.6 ppmv lower than that in the CTRL, with proportionate declines in EXP2 (-5.1 ppmv) and EXP3 (-20.8 ppmv). Table 2 also presents global mean sur-

face air temperature (SAT) to provide an indication of the climate impact of these xCO_2 changes. For EXP1, the lowered xCO_2 translates to a decrease in SAT of -0.06°C compared to the CTRL simulation, averaged over the 2090s.

The final block of Table 2 reports wider measures of marine biogeochemistry, including net primary production (NPP), export of organic and inorganic carbon, and surface carbonate chemistry properties. Unlike major carbon cycle properties, which respond in consistent patterns and appropriate magnitudes between experiments, changes in these quantities can be less consistent. For instance, NPP and organic carbon export vary both positively and negatively across the experiments by the 2090s, with magnitudes that are inconsistent with the magnitude of the OAE perturbation. However, and unsurprisingly, biogeochemical properties specifically associated with carbonate chemistry consistently track OAE. Both surface pH and calcite saturation state ($\Omega_{calcite}$) are slightly increased by OAE against the ongoing ocean acidification. In MEDUSA, $\Omega_{calcite}$ affects the simulated biogenic production of inorganic carbon, and the export flux of $CaCO_3$ both increases in response to OAE, and with a greater magnitude than the changes in organic carbon.

To complement the globally-integrated time-series and metrics, Figure 3 shows the geographical distribution of changes in TA and DIC found in EXP1, while Table 5 summarises patterns in Δ TA and DIC for the major ocean basins. Panels 3a and 3b respectively show 2090s mean surface TA and DIC in the CTRL simulation. The corresponding difference in TA and DIC concentrations in EXP1 are shown in panels 3c and 3d. The geographical patterns of Δ TA and DIC are highly correlated, with the highest positive concentrations occurring in the Indonesian / Malaysian archipelago, where shelf area and sea temperatures are greatest. As indicated in Table 5, concentrations of Δ TA are most elevated in the Atlantic (+26.2 meq m^{-3}) and, especially, Indian basins (+39.1 meq m^{-3}), with lower concentrations in the Pacific (+9.3 meq m^{-3}) and Southern basins (+5.4 meq m^{-3}). Meanwhile, both the Southern and, especially, Pacific basins have regions where the concentrations of Δ TA and DIC are actually negative, with higher local concentrations in the CTRL simulation. In the Pacific Ocean, these regions are in the north and west of the basin, relatively remote from areas of OAE or where upwelling of older watermasses is more important.

Panels 3e and 3f show the corresponding geographical distributions of vertically-integrated Δ TA and DIC. These integrals are greatest in the North Atlantic, and lowest in the tropical Pacific and Southern Ocean. In the North Atlantic, this pattern is driven by the combination of relatively high OAE at its margins, coupled with large-scale circulation and deep water formation in the northern part of this basin. Because of the shared physical mechanism, this pattern has similarities with that of anthropogenic CO_2 in the present-day ocean (Key et al., 2004). By contrast, the situation in the Southern Ocean, another major sink of anthropogenic CO_2, diverges because of the relatively low OAE at its margins. Overall, the patterns of Δ TA and DIC storage within the ocean convolute the locations of OAE with general circulation and ventilation of the ocean's interior.

Note that the Pacific and Indian metrics in Table 5 are distorted by the high OAE inputs in the Indonesian / Malaysian archipelago region. This region is designated Pacific in Table 5, but a large fraction of OAE additions there are transported through the Indonesian Throughflow into the Indian where they contribute both to elevated surface and vertically-integrated Δ TA (and DIC) in this basin rather than the Pacific.

Expanding on Figure 3's vertical integrals of TA and DIC, Figure 4 presents their corresponding geographical and vertical patterns. These are illustrated by means of "thermohaline transect" plots that present a continuous zonal mean section (i.e. east-west average) that runs from the Arctic Ocean (left), southward down the Atlantic Ocean to the Southern Ocean and Antarctica (centre), before running northward up through the

Pacific Ocean to the Bering Strait (right). In the CTRL panels, 3a and 3c, this shows the lower TA and DIC concentrations characteristic of the younger North Atlantic Deep Water (NADW), higher concentrations of the Southern Ocean and the Antarctic Bottom Water (AABW) formed around it, and the highest concentrations in the oldest watermasses of the North Pacific. This pattern of progressive enrichment reflects watermass age (i.e. time since ventilation), and the dissolution and remineralisation of TA and DIC mediated by the natural biological pump.

Panels 3b and 3d show the respective differences in TA and DIC concentrations in EXP1. Fitting with its long ventilation age, the majority of the ocean interior shows no signal of the 80-year duration of simulated OAE. However, surface concentrations of both TA and DIC are elevated, particularly in the Atlantic Ocean (per Table 5). As expected, concentrations in the Southern Ocean are low, since this region is both limited in shelf area, and has a hydrographic circulation that draws in deep water relatively unaffected by OAE. Meanwhile, in the Atlantic Ocean, and in the connected Arctic Ocean, significant concentrations of TA and DIC have reached greater depths. Deep mixing in the northern North Atlantic (40°–60°N), as well as the formation of NADW in this region, has transported both down to depths of 2000 m. While zonal mean surface concentrations are low, or even negative, in the open Arctic Ocean, the basin's large shelf regions and the intrusion of North Atlantic Current waters from the south elevate interior concentrations down to 1000 m.

Figure 5 focuses back to the ocean's uptake of CO_2, and how this relates to the spatial application of OAE. Panel 5a shows the geographical patterns of integrated CO_2 air-sea flux over the entire period of the CTRL simulation. The main features are high fluxes into the ocean at high latitudes, especially into Southern Ocean, and modest outgassing fluxes at low latitudes, most noticeably the equatorial Pacific Ocean. Meanwhile, Panel 5b shows the corresponding change in air-sea flux found by EXP1. Here, the fluxes are relative to the CTRL, such that "ingassing" may actually be *less* "outgassing", and vice versa. In this, the most pronounced features are the additional ingassing in OAE regions, especially in the Indonesian / Malaysian archipelago, and in adjacent downstream areas. Noticeably, although OAE is focused around the continental margins, the wider open ocean in EXP1 experiences changes. Further, although OAE is an addition of TA that should drive an increase in CO_2 uptake by the ocean, there are relatively large areas where the impact of OAE appears to decrease this uptake. The most significant of these regions are found at high latitudes, in the northern Atlantic and Pacific oceans and in the Southern Ocean. These regions have relatively strong ingassing in the CTRL simulation, so these changes in EXP1 make them regions of slightly *lower ingassing*. Away from these regions of focused ingassing decline, the wider open ocean generally exhibits patchiness, with large regions ($>$ 1000 km) showing slight positive or slightly negative changes to CO_2 air-sea flux.

Table 3 summarises the patterns of integrated CO_2 air-sea flux by first breaking them down into shelf and open ocean regions, and then by whether they are net ingassing or outgassing when time-integrated. In the simulations here, the total area of the grid cells in which OAE occurs is 10.2% of the total domain (of which 55.4% is the fractional area that experiences OAE), and in the CTRL simulation this is responsible for 7.37% of the total air-sea CO_2 flux integrated 2020–2100. Unsurprisingly given OAE, the corresponding shelf fraction of air-sea CO_2 flux in EXP1 increases to 10.1%, with the other experiments similarly showing an increase. However, in all cases, the off-shelf uptake of CO_2 also increases, by 3.33% compared to the CTRL in EXP1. When the CTRL air-sea CO_2 flux is separated from the experiments to calculate Δ fluxes, and then the change in CO_2 uptake is compared between shelf and off-shelf regions, the two regions show an approximately equal share occurs in both regions. In the case of EXP1, 47.9% of the additional CO_2 uptake occurs in the off-shelf region away from the shelf area where OAE is in operation, and this split is similar across all of the experiment simulations. Sections

(c) and (d) of Table 3 further show that, if regions are divided into those where the Δ fluxes are of opposite sign, the dominance of off-shelf CO_2 uptake is even greater, 55.4% in EXP1. This increase in the importance of off-shelf regions is offset, however, by areas of decreased ingassing. Overall, Table 3 underscores that a significant fraction of the additional CO_2 uptake driven by OAE actually occurs off-shelf, away from the application zone.

Finally, Figure 6 and Table 4 describe the stoichiometric relationship between the addition of TA and the absorption of DIC. Panels 6a and 6b respectively show the (Δ DIC):(Δ TA) ratios of surface waters and water column integrals. As noted previously, because some regions of the experimental simulations actually show *lower* TA or DIC than the CTRL, this can result in a negative relationship, and these areas are blanked. Inevitably, this being a ratio, where Δ TA or Δ DIC approach near-zero values, it is distorted either towards extreme values, most clearly seen at the periphery of the blanked regions. In general, regions more strongly affected by the simulated OAE, such as the Atlantic and Indian oceans, show (Δ DIC):(Δ TA) between 0.5 and 1.0, with less affected regions, such as the western Pacific and Southern oceans, showing these more extreme values already alluded to. Of which, neighbouring regions of both extremely high and extremely low ratios can be found bordering low or negative Δ TA or Δ DIC in the Southern Ocean.

Integrating the horizontal distributions of Δ TA and Δ DIC to vertical profiles, Panel 6c describes their relationships with depth for EXP1 and rate sensitivity experiments EXP2 and EXP3. All three experiments show the same general patterns of declining concentrations of both properties with depth, and consistently lower Δ DIC than Δ TA. Panel 6d shows EXP1 only, and uses a two-dimensional histogram of integrated ocean volume to illustrate the relationship between the grid cell concentrations of Δ TA and that of Δ DIC. As noted previously, the majority of the ocean volume contains negligible Δ TA and Δ DIC, and the origin point of Panel 6d (0 ± 2.5 mmol m^{-3}) contains 84.4% of the ocean's total volume. Of the rest of the ocean's volume, the majority ($> 95\%$) has positive values of Δ TA and Δ DIC and lies generally along an axis in which both covary. Panel 6d shows both the 1:1 line, and a simple linear regression (using grid cell volume weighting) of the two quantities. Table 4 reports the slope of the latter as 0.800 ($r^2 = 0.922$), but at the high ends of both quantities are regions with clearly divergent slopes, higher and lower than that of the regression. The significant divergent regions marked with numbers on Panel 6d are: 1. Caspian Sea and Baltic Sea; 2. Persian Gulf; 3. Gulf of Thailand and Gulf of Carpentaria; 4. Bohai Sea; 5. western North Pacific; 6. Bering Sea; 7. central Arctic Ocean. These extreme or anomalous regions are broadly confined to the ocean's surface mixed later (shallower than 100m), with the exception of the western North Pacific and Bering Sea regions, which are generally interior (60–600m) and without surface contact. Regions 1–4 are also geographically confined within inland seas (e.g. Caspian Sea) or cul-du-sac areas of the model grid (e.g. Baltic and Bohai seas). Note, however, that although most of these regions are anomalous with respect to the general quasi-linear relationship between Δ TA and Δ DIC, they are not quantitatively significant in terms of ocean volume.

3.1 Sensitivity experiments

The release rate sensitivity experiments aim to quantify the linearity of the response of the simulated OAE, with idealised half and double rates that essentially break the assumptions of the OAE equation. As Table 2 shows, across the main TA and DIC metrics, EXP2 and EXP3 almost linearly track EXP1. The changes in surface concentrations in both approximate the halving and doubling of OAE, for the 2020s and, particularly, the 2090s. By 2100, the global inventory of ocean TA has been increased by 2.330 Peq in EXP1, with EXP2 50.1% and EXP3 199.4% of this, while ocean DIC has increased in response by 1.814 Pmol in EXP1, with EXP2 50.7% and EXP3 197.7%. Ocean car-

bonate chemistry – pH, $\Omega_{calcite}$ – shows similar well-aligned responses between the experiments, although the patterns across other important marine biogeochemistry metrics – NPP, C_{org} export, $CaCO_3$ export – are more inconsistent. The atmospheric response across the simulations also presents a somewhat linear picture, with EXP1's -9.607 ppmv decline in xCO_2 aligning with -5.148 and -20.816 ppmv in EXP2 and EXP3 respectively. However, the relatively small change in 2090s mean SAT in EXP1 is much less well-aligned, with EXP2 showing no change at all from the CTRL, and EXP3 showing a change almost 4 times as large. Overall, the results here suggest a broadly linear response in the variables most immediately affected by OAE, but with much less clear alignment in more indirectly affected variables.

The release depth sensitivity experiments aim to understand the sensitivity of results to the model's limited vertical resolution, specifically that grid cells necessarily have a single depth, while the real world space they represent includes seafloors across a range of depths. While EXP1 uses a fixed depth of 100m (or shallower where necessary), simulated OAE could have a profile that tries to represent this real world range, but here we consider two end-members – 0m and 200m – that instead bracket this range. Again using the results in Table 2, EXP4 and EXP5 are found to be broadly similar, but with divergences that generally align with the expectation that shallow OAE should have the greatest effect because its TA introduction is closest to the atmosphere's CO_2. Surface concentrations of DIC in both the 2020s and 2090s hint at this, but with relatively small discrepancies. However, the global inventory of DIC by 2100 shows the experiments align with EXP4 having the greatest additional CO_2 uptake, EXP5 the lowest, and with EXP1 sitting in-between. EXP4 has 11.0% more uptake than EXP1, while EXP5 has 3.3% less, and this is reflected in atmospheric xCO_2 change, with EXP5's deep OAE release being less efficient. The year 2100 ratio of Δ DIC to Δ TA – 0.779 in EXP1 – is 0.863 in EXP4 and 0.750 in EXP5. Overall, the results suggest a sensitivity to the way in which the effects of OAE are imposed in the model, although the use of end-members here will tend to exaggerate this.

4 Discussion

In this study, we have used a state-of-the-art Earth system model, UKESM1, to evaluate the potential significance of a coastal ocean alkalinity enhancement scheme for abating the impacts of anthropogenic climate warming. The coastal approach used in this scheme makes access and delivery issues easier to address than open ocean schemes, and facilitates the retention of the dissolving mineral source of TA in close proximity to the atmospheric CO_2. OAE is simulated here by introducing a supply of total alkalinity in coastal waters at 100m for the period 2020-2100, using temperature-dependent dissolution of a layer of olivine sand deposited on the seafloor. This additional TA is tracked together with its impact on ocean concentrations of dissolved inorganic carbon – the focus of OAE schemes – and on wider properties such as ocean pH, atmospheric xCO_2 and air temperature. Over the simulation duration, the addition of 2.33 Peq of TA via OAE leads to the extra absorption of 1.81 Pmol of DIC (i.e. a ratio of 1 eq : 0.78 mol C), resulting in an atmospheric xCO_2 difference of -9.61 ppm and a global mean surface air temperature difference of -0.06°C. Although TA is only added in shallow coastal regions here, almost half of the additional CO_2 (47.9%) uptake by the ocean actually occurs elsewhere due to the added TA being advected off the shelf areas. While the OAE scheme acts to increase ocean TA, chaotic dynamics and interactions with the modelled production of calcium carbonate (which acts to decrease surface TA) mean that some regions actually show lower concentrations of TA and DIC than the control simulation, and lower CO_2 ingassing. Sensitivity experiments on the addition rate of OAE find a generally linear response between TA added and extra DIC absorbed, while end member experiments on the depth of TA addition find that increasing release depth decreases absorption efficiency.

A key metric of the efficacy of OAE schemes is its absorption efficiency – the quantity of additional DIC stored in the ocean per the amount of TA added by that scheme. In terms of this metric, the global mean value found here of 0.78 is comparable to other modelling studies, despite a number of methodological differences and approaches to simulating OAE. The lowest integrated values reported were from Butenschön et al. (2021)'s Mediterranean study, where efficiency reached 0.5 after 30 years of OAE operations. The global study of Burt et al. (2021) found an efficiency of 0.70 when OAE was applied globally, but higher values when the same quantity of activity was focused regionally, up to 0.89 in the case of Southern Ocean applications. Meanwhile the decade-scale, localised Bering shelf study of Wang and Dreisinger (2022) found this efficiency to rise from 0.46 in year 1 to 0.95 by year 10. In terms of comparable global studies with coastal releases, in their simulation with the greatest absolute CO_2 drawdown, Feng et al. (2017) found an efficiency of 0.60 (rising to 0.72 with lower TA additions), while He and Tyka (2023) found that, after initially lower efficiency, this rose to 0.8 after 3–4 years of simulation. The elevated efficiency with lower TA additions found by Feng et al. (2017) would suggest that the near-linear response to OAE found in this study is a consequence of the much lower TA additions here. For reference, in the analogous laboratory study of runaway $CaCO_3$ precipitation using quick lime rather than olivine, Moras et al. (2022) estimated a maximum efficiency of 0.8 in experiments.

As an aside, even if OAE TA is not responsible for DIC absorption prior to its subduction, ocean circulation will eventually return it to the surface ocean on longer timescales (decadal, centennial, millennial), at which point it may then absorb more carbon. Essentially, OAE is increasing the long-term capacity of the ocean to store DIC, even if, in the short-term, this potential is not realised. That said, the principle value of OAE is in increasing CO_2 absorption during the 21st century, and not at some hypothetical future time when an OAE-enriched watermass is ventilated. Related to this, a difficult-to-quantify component of the efficiency of OAE is its potential impact on biological pump carbon away from the surface. Carbon associated with this natural pump is unbuffered and outgases when the watermass that it is associated with is ventilated (e.g. in the Equatorial Pacific upwelling region). However, should OAE TA be subducted away from the surface of the ocean before it becomes associated with the absorption of addition DIC in the surface ocean, it could buffer this carbon which would otherwise be unbuffered (and might even hint at an alternative approach to OAE). However, the significance of this process would be extremely challenging to quantify so is beyond this study.

Important considerations for OAE are the practical requirements of the olivine distribution implied in this study, in particular the quantity of material required to achieve the results found. In EXP1, 2.330 Peq of TA are dissolved into the ocean over the 80 simulation years (Table 2). Assuming that the dissolution of each mol of olivine results in the production of 4 eq of TA (Köhler et al., 2010), to add this quantity of TA to the ocean would require 0.5825 Pmol of olivine. Assuming a molar mass of 140 g mol^{-1} for olivine (Feng et al., 2017), this translates to 81.55 Pg of olivine, or approximately 1 Pg of olivine per year based on the application methodology used here. The mining estimates of Feng et al. (2017) suggest that annual olivine extraction is approximately 70 Tg, which would provide less than 7% of that required for the operation of the OAE scheme explored here. While an extreme (more than an order of magnitude) increase in mining would be required to satisfy this demand, it is also important to note that olivine is a widely available mineral, and that – for a crude comparison – the 1 Pg y^{-1} required is considerably smaller than the 8 Pg y^{-1} of coal mined annually (IEA, 2022), a mineral whose requirement for mining will necessarily decline to achieve net zero. Aside from the primary consideration of the availability of olivine, its processing, transportation and distribution at coastal locations imply further practical constraints that are beyond this study. Some aspects of these are quantified in the coastal OAE study of He and Tyka (2023).

Another important consideration for the practical deployment of OAE is its monitoring in the field. Tracking the TA added and measuring downstream consequences such as additional DIC absorbed and changes in carbonate chemistry properties is a major component of proposed schemes. This is both to identify potential unintended consequences or impacts (e.g. to marine ecosystems), and to verify that the activity has had the intended result of CO_2 absorption. The work here highlights several difficulties in this regard. First, added TA and extra DIC are distributed far from the location of OAE operations (e.g. Figure 3), including to great depth (e.g. Figures 4 and 6). Bar an initial period of local observation, basin- or global-scale programmes capable of both surface and interior measurement would be necessary if monitoring its full effects was an operational requirement. Second, approximately half of the extra DIC induced by OAE to enter the ocean is absorbed in ocean areas outside of that of OAE operations. This is potentially even more significant since determining the magnitude of this absorption is critical for justifying – and, potentially, financially-driving – OAE. Third, across a large region of the ocean's surface the concentrations of added TA and extra DIC that result in this study are approximately 2.5% of background concentrations (i.e. $\approx$50 mmol m^{-3} compared to $\approx$2000 mmol m^{-3}; Figure 3), while measurement errors are typically larger. For instance, the recent methodology of Vesper et al. (2015) finds a measurement error of 4.4% (and natural variability will further complicate separation of signal from noise). Echoing Wang and Dreisinger (2022)'s conclusion from their localised Bering shelf study, this global-scale dispersal, CO_2 uptake away from operational areas, and low signal magnitude relative to measurement precision underscore that modelling approaches will be critical for evaluating many details of OAE schemes.

Finally, an aspect hinted in the earlier analysis is the variability in the absolute absorption of CO_2 across the operational area of OAE simulated. In large part, this stems from the input of TA in the first place, with warmer tropical regions with large shelves especially important (but see immediately below). To attempt to quantify this, Figure 7 sorts grid cells within the OAE operational area by CO_2 absorbed, and then integrates them to determine the fractional importance of different coastal areas. Of the total OAE area examined, 13.8% is responsible for 50% of the total CO_2 flux (and 50.7% for 90% of the flux). Geographically, "hotspots" of OAE efficiency (red regions of Figure 7b) are primarily located in the vicinity of the Indonesian Throughflow (e.g. Gulf of Thailand, the Timor, Arafura and Coral seas), with other significant regions dotted around the world (e.g. Gulf of Mexico, Arabian Sea, Persian Gulf, Yellow Sea). Many other coastal regions (cyan regions of Figure 7b) are much less important, even where they include large areas of ostensibly suitable coastal shelf (e.g. North Sea, North American Eastern Seaboard, Arctic Ocean, Patagonian Shelf). These results suggest that OAE activity of the kind envisaged here would benefit from targeted focusing, and that a relatively small area of the Earth's global shelf could achieve most of its benefits (but see the next section's caveats). As an aside, it is noticeable that much of the OAE capacity simulated here lies within marine areas associated with "Global South" nations. This potentially opens up a new revenue stream for such countries, but also raises the spectre of exploitation by developed nations (cf. fisheries; Belhabib & Le Billon, 2022), so any such use of OAE should require proper engagement with local communities and authorities (e.g. Gurney et al., 2021).

In the above analysis, note that the area definition used specifically excludes the significant quantity of CO_2 that is absorbed outside of the OAE operational areas (47.9% of the global total; Table 3). This results in some major shelf regions (e.g. Amazonian Shelf) appearing comparatively less important because they exhibit a higher rate of off-shelf advection of the added TA (i.e. the local shelf retention is lower). Accounting for their true significance by including off-shelf CO_2 uptake is not straightforward in the kind of simulations here, however, because it is challenging to segregate *in-situ* and remote (downstream) off-shelf extra CO_2 uptake. An alternative modelling approach that could assist with the attribution for OAE is Lagrangian particle-tracking. This simulates the

transport of passive particles within the model's circulation field and allows the connectivity of ocean regions to be determined (e.g. Robinson et al., 2017; Popova et al., 2019). By tracking the fate of such particles after their release from OAE operational areas, such an approach could be used to quantify the shelf retention and export of added TA (e.g. van Gennip et al., 2017). However, this approach also has its own distinct limitations that preclude it from working in the framework here (e.g. low grid resolution), and so is not pursued here.

4.1 Limitations and future directions

Obvious limitations of this study are its use of a single ESM (UKESM1), a single future emissions scenario (SSP585), a single OAE strategy (global shelf operations, constant release 2020-2100), and limited sensitivity analysis along two idealised avenues (OAE rate, OAE depth).

The limitations imposed by using only a single model are challenging to overcome because of the significant requirements, in terms of both human and computational resources, to operate even a single model. The CDRMIP project (Keller et al., 2018) provides a standardised OAE experiment protocol for ESMs taking part in CMIP6, with the aim that a single experimental design can be simulated for any model. The CDRMIP protocol differs from that used here, framing OAE as a truly global ocean activity, with TA added everywhere across the ocean rather than focused on OAE in coastal regions, as here. However, even with the support of CMIP6, only a single model has archived output with the Earth System Grid Federation (ESGF) for CDRMIP as of 08 July 2023. Nonetheless, CDRMIP offers a practical template for entraining ESMs into common experiments where different uncertainties, such as ocean physical and biogeochemical dynamics, can be evaluated and quantified. Currently, CDRMIP only considers a single OAE scenario (with a single sensitivity experiment in which it is switched off after a period of use), but a coastal release experiment, akin to that examined here, could be a future extension. And though a fully-coupled – and computationally-expensive – ESM has been used here to investigate feedbacks to atmospheric xCO_2 and SAT, the magnitude of these may be small enough that significantly less expensive forced ocean-only experiments may be valuable where there is a greater focus on ocean-side processes (e.g. carbonate chemistry, ocean acidification, ecological impacts, etc.).

A specific uncertainty introduced by the biogeochemical model used here, MEDUSA, lies in its alkalinity cycle. This parameterises a relationship between the solubility of $CaCO_3$ and its biological production, and ties this production to the export flux of both organic and inorganic carbon via a ballast parameterisation (Armstrong et al., 2001). Against a background of decline due to ocean acidification, OAE acts to promote $CaCO_3$ production in MEDUSA, increasing its export of both inorganic carbon and TA, and leading to (ballasted) sinking organic carbon reaching greater depths before remineralisation. However, the factors governing the production and export of $CaCO_3$, as well as the relationship between $CaCO_3$ and the sinking flux, remain uncertain, and the response of associated organisms is highly variable (Kroeker et al., 2013). As a result, models vary significantly in their representation of these aspects of marine biogeochemistry (Planchat et al., 2023), and other models may exhibit different responses to those of MEDUSA. Of which, as Table 2 shows, while $CaCO_3$ production clearly responds positively to OAE, the relationship with export production is less straightforward. Future work spanning a range of biogeochemical models and different underlying assumptions, for instance wider CDRMIP participation, would help clarify the likely significance of such feedbacks from OAE activities.

Regarding the scenario chosen, SSP585, this has high CO_2 emissions, and represents a much less desirable outcome than that planned under the Paris Agreement. As such, the drop in atmospheric xCO_2 (-9.6 ppm; Table 2) caused by OAE appears small

compared to its background rise (447.0 ppm, 2020s → 1118.4 ppm, 2090s) across the CTRL simulation. However, such a change would be more significant under preferred future scenarios with lower xCO_2 rise, although this might not be entirely realised were the air-sea xCO_2 gradient to be lower under such a scenario. Consequently, the use here of a single future scenario leaves some uncertainty on the relative effectiveness of OAE should actual future xCO_2 track the lower (e.g. SSP126) or higher (e.g. SSP585) scenarios. It has recently been suggested by (Ho, 2023) that technologies such as OAE are at their most effective when emissions are reduced to just those that are difficult to abate (≈18% of current emissions; Buck et al., 2023), and thus more likely relevant for low emissions scenarios that tackle net zero considerations more effectively.

An important simplification here is the use of a temperature-dependent approximation of olivine sand dissolution. Most other OAE studies simulate the addition of TA to the ocean at a prescribed rate (e.g. Feng et al., 2016; Köhler, 2020; Burt et al., 2021; Butenschön et al., 2021), and this is also the approach of CDRMIP (Keller et al., 2018). The pioneering study of Ilyina et al. (2013) instead explicitly links TA addition via OAE to contemporaneous emissions of CO_2, allowing OAE to proportionately track different projections. Meanwhile, the comprehensive study of Feng et al. (2017) prescribes the addition of basic minerals to the ocean, but estimates the dissolution of these minerals to TA as a function of mineral grain size and ambient temperatures and pH. Here, our TA input function simplifies this to the temperature-dependent rate of dissolution of a thin layer (1 cm) of olivine sand with a fixed grain size (250 μm) and fixed porewater pH. As such, the quantity of olivine sand ultimately required to satisfy this dissolution is dynamic and varies in both space and time (and, additionally, with climate warming). Nonetheless, considerable uncertainty remains around actual TA addition, including from the precise minerals involved (as noted at OAE's inception; Kheshgi, 1995), the dissolution dynamics of particles (e.g. Feng et al., 2017), and the resulting chemical kinetics (e.g. Moras et al., 2022; Hartmann et al., 2023). As found during recent field trials, consideration even needs to be taken of seafloor sediment dynamics in case OAE minerals are buried by tidal or current processes (Tollesfon, 2023).

The details of the implementation of coastal OAE used here involve a number of other simplifications. We assume that the addition of olivine sands to the coastal zone only occurs in regions of depth up to 100 m, but that these are applied on a global basis. This obviously immediately overlooks the potential hazard such activity would likely pose to seafloor ecosystems, such as sediment smothering by the applied olivine sands (e.g. Pineda et al., 2017). In particular, ecosystems founded around benthic or attached autotrophs, such as seagrass (UNEP-WCMC & Short, 2021) or kelp (Jayathilake & Costello, 2020), would likely be affected, and these are also independently being considered for CO_2 removal (e.g. Oreska et al., 2017; Coleman et al., 2022). However, this simplified approach also overlooks a number of practical factors including: 1. their proximity to suitable sources of olivine capable of being mined; 2. their proximity to land-side (e.g. roads) and ocean-side (e.g. ports) intrastructure; 3. the physical accessibility of the coastal regions (e.g. for dispersal operations); 4. the occurrence of coastal hazards (e.g. sea ice, icebergs, treacherous bathymetry); 5. competition with existing marine activities (e.g. fisheries, commercial, leisure); 6. issues of national sovereignty (e.g. where neighbouring states disagree on OAE use). The model scheme also essentially assumes a constant supply of olivine sands to OAE areas, without considering any seasonal factors that might impede this, such as seasonal marine activities (e.g. fisheries and leisure in populated regions), or other natural factors (e.g. day length and ice hazards at high latitudes). While factors such as these were considered in the experimental design, the many uncertainties associated with them favoured a simplified approach that served as an end member of the efficacy OAE should all such impediments be overcome. The analysis of He and Tyka (2023) includes an evaluation of the complexity of such calculations, including how transportation costs combine with the molar ratio of CO_2 uptake per unit mass of OAE substrate to affect the overall cost (e.g. per tonne of CO_2).

A further aspect overlooked here are the potential consequences of terminating the activity, for instance, should unforeseen negative consequences occur (e.g. natural ecosystem changes). This aspect is explicitly considered in the CDRMIP protocol, with a sensitivity simulation, *esm-ssp585-ocn-alk-stop*, in which OAE activity stops from year 2070 onward. This design permits the examination of important considerations for the application of OAE, such as potential changes to and then recovery of natural ecosystem function. In their exploration of OAE termination, Ilyina et al. (2013) note that because TA addition to the ocean is essentially permanent (at least in this model; and also in MEDUSA), the CO_2 drawdown of OAE activity would persist and not reverse. This would mean that, unlike some geoengineering interventions (e.g. solar radiation management; Tilmes et al., 2015), use of OAE does not require an ongoing commitment.

Finally, as noted earlier, the dynamics of ESM models such as that used here mean that simulations rapidly diverge, introducing confounding effects that are reduced in Results by simply using decadal-scale averages to "smooth out" the resulting variability. However, a superior approach would be to simulate multiple ensemble members of both the control and experiment simulations, and use the means of these to reduce the significance of this "noise". This could be achieved, for instance, by repeating all of the simulations here using initial conditions that branch from different time-points of the original piControl simulation. As described in Sellar et al. (2019), UKESM1's ensemble of Historical period simulations followed such an approach, using initial time-points that were selected to be well-separated in terms of Inter-decadal Pacific Oscillation (IPO; Power et al., 1999; Zhang et al., 1997) and Atlantic Multi-decadal Oscillation (AMO; Kerr, 2000) variability. However, as the simulations here were already computationally expensive (including in CO_2 emissions), while this would increase their robustness, the central results would not likely be significantly affected.

In terms of future activity, a number of points are suggested (or reiterated) by this study. Currently, most studies of OAE – and this one is no exception – involve bespoke parameterisations (input quantity, geographical distribution, experiment background / duration), making cross-comparison challenging. CDRMIP presents a common alternative, although it currently establishes a global-scale, open ocean OAE protocol that, as yet, has not been widely-adopted and simulated across the ESM community. While challenging to establish, a less idealised protocol that better reflects likely field trials or developments in OAE may assist here, and the upcoming CMIP7 presents a pertinent timescale for its development. Such a protocol could additionally serve to establish a common methodology for quantifying the "efficiency" of OAE, including the wider storage and redistribution of CO_2 absorbed away from release locations. This study found that separation of added TA and extra DIC was complicated by the internal variability of the model used, so having an established method for resolving this is desirable. Finally, while OAE experiments are typically well-documented in the literature, relevant details of the underlying biogeochemistry models in which they are embedded are often overlooked. The wide range in model complexity used across the discipline (e.g. Kwiatkowski et al., 2020; Séférian et al., 2020) includes a corresponding range in how TA and DIC are represented and how they interact with the model's wider biogeochemistry (Planchat et al., 2023). For example, the model used here, MEDUSA, explicitly links carbonate chemistry to its biological pump, with the potential for OAE to alter this (although Table 2 suggests only a minor effect).

5 Conclusions

- Here we examine ocean alkalinity enhancement using a state-of-the-art Earth system model (UKESM1) with global-scale coastal addition of alkalinity equivalent to that from a continuously-replenished 1 cm layer of olivine to shelf regions shallower than 100 m.

- The simulated OAE has an impact on CO_2 air-sea flux, increasing absorption rate by an average 0.3 Pg C y^{-1} over the study period (2020–2100), corresponding to a total of 24 Pg C removed from the atmosphere by the effect of the olivine dilution (approximately what is currently released into the atmosphere in ≈2 y).
- The depth at which alkalinity added by olivine dissolution has small impact on the CO_2 flux (suggesting strong mixing), although the absolute rate of alkalinity addition matters with an quasi-linear impact on the CO_2 air-sea flux increase.
- In the default simulation, EXP1, the overall impact on atmospheric CO_2 concentration is a decrease of 10 ppm relative to the control, which mitigates increasing surface air temperature by -0.06°C by 2100, well within the noise of the SAT increase between 2020-2100.
- Although added on the shelves, the alkalinity is redistributed globally by ocean currents within the period of the experiment, and around 50% of the extra DIC absorbed does so off-shelf — with significant implications for the monitoring, reporting and verifying of the efficacy of this OAE approach.
- The amount of olivine needed for these results can be deduced from the total alkalinity added (2.3 Peq), and corresponds to 81 Pg of olivine over the simulation period, or about 1 Pg per year – which is more than 14 times the current global production of olivine.

Open Research Section

The subset of output from model simulations used in the preparation of this manuscript have been placed in a Zenodo archive (Yool & Palmieri, 2023). This includes netCDF files of 2D and 3D geographical output and text files of globally-integrated variables produced by the BGCVal evaluation software (de Mora et al., 2018).

Acknowledgments

The authors would like to thank Katya Popova (National Oceanography Centre), Colin Jones (University of Leeds), Andy Wiltshire (UK Met Office), Chris Pearce (National Oceanography Centre) and Chelsey Baker (National Oceanography Centre) for invaluable input and comments on the manuscript. The authors are grateful to Olivier Sulpis (Project Vesta; CEREGE) for supplying the function for olivine dissolution used in this study (Equation 2). The authors would also like to thank Steve Romaniello and Grace Andrews (Project Vesta) for providing relevant background information about coastal ocean alkalinity enhancement.

This work was funded by the UK National Environmental Research Council (NERC, UK) under the following projects: 1. National Capability Science Multi-Centre (NCSMC) funding for Future Impacts, Risks and Mitigation Actions in a changing Earth system project (TerraFIRMA LTSM; NE/W004895/1); 2. National Capability Science Multi-Centre (NCSMC) funding for the UK Earth System Modelling project (ESM LTSM; NE/N018036/1); 3. National Capability Science Single-Centre (MCSSC) funding for the Climate Linked Atlantic Sector Science project (CLASS LTSS; NE/R015953/1).

References

Albright, R., Caldeira, L., Hosfelt, J., Kwiatkowski, L., Maclaren, J. K., Mason, B. M., ... Caldeira, K. (2016). Reversal of ocean acidification enhances net coral reef calcification. *Nature*, *531*, 362–365. doi: 10.1038/nature17155

Armstrong, R. A., Lee, C., Hedges, J. I., Honjo, S., & Wakeham, S. G. (2001). A new, mechanistic model for organic carbon fluxes in the ocean based on the quantitative association of poc with ballast minerals. *Deep Sea*

Research Part II: Topical Studies in Oceanography, *49*(1), 219–236. Retrieved from https://www.sciencedirect.com/science/article/pii/S0967064501001011 (The US JGOFS Synthesis and Modeling Project: Phase 1) doi: https://doi.org/10.1016/S0967-0645(01)00101-1

Belhabib, D., & Le Billon, P. (2022). Fish crimes in the global oceans. *Science Advances*, *8*, eabj1927. Retrieved from https://www.science.org/doi/abs/10.1126/sciadv.abj1927 doi: 10.1126/sciadv.abj1927

Buck, H. J., Carton, W., Lund, J. F., & Markusson, N. (2023). Why residual emissions matter right now. *Nature Climate Change*, *13*, 351–358. doi: 10.1038/s41558-022-01592-2

Bullock, L. A., Yang, A., & Darton, R. C. (2022). Kinetics-informed global assessment of mine tailings for co_2 removal. *Science of The Total Environment*, *808*, 152111. Retrieved from https://www.sciencedirect.com/science/article/pii/S0048969721071874 doi: https://doi.org/10.1016/j.scitotenv.2021.152111

Burt, D. J., Fröb, F., & Ilyina, T. (2021). The sensitivity of the marine carbonate system to regional ocean alkalinity enhancement. *Frontiers in Climate*, *3*. Retrieved from https://www.frontiersin.org/articles/10.3389/fclim.2021.624075 doi: 10.3389/fclim.2021.624075

Butenschön, M., Lovato, T., Masina, S., Caserini, S., & Grosso, M. (2021). Alkalinization scenarios in the mediterranean sea for efficient removal of atmospheric co_2 and the mitigation of ocean acidification. *Frontiers in Climate*, *3*. Retrieved from https://www.frontiersin.org/articles/10.3389/fclim.2021.614537 doi: 10.3389/fclim.2021.614537

Coleman, S., Dewhurst, T., Fredriksson, D. W., St. Gelais, A. T., Cole, K. L., MacNicoll, M., ... Brady, D. C. (2022). Quantifying baseline costs and cataloging potential optimization strategies for kelp aquaculture carbon dioxide removal. *Frontiers in Marine Science*, *9*. Retrieved from https://www.frontiersin.org/articles/10.3389/fmars.2022.966304 doi: 10.3389/fmars.2022.966304

de Mora, L., Yool, A., Palmieri, J., Sellar, A., Kuhlbrodt, T., Popova, E., ... Allen, J. I. (2018). Bgc-val: a model- and grid-independent python toolkit to evaluate marine biogeochemical models. *Geoscientific Model Development*, *11*(10), 4215–4240. Retrieved from https://gmd.copernicus.org/articles/11/4215/2018/ doi: 10.5194/gmd-11-4215-2018

Eyring, V., Bony, S., Meehl, G. A., Senior, C. A., Stevens, B., Stouffer, R. J., & Taylor, K. E. (2016). Overview of the coupled model intercomparison project phase 6 (cmip6) experimental design and organization. *Geoscientific Model Development*, *9*(5), 1937–1958.

Feng, E. Y., Keller, D. P., Koeve, W., & Oschlies, A. (2016, jul). Could artificial ocean alkalinization protect tropical coral ecosystems from ocean acidification? *Environmental Research Letters*, *11*(7), 074008. Retrieved from https://dx.doi.org/10.1088/1748-9326/11/7/074008 doi: 10.1088/1748-9326/11/7/074008

Feng, E. Y., Koeve, W., Keller, D. P., & Oschlies, A. (2017). Model-based assessment of the co_2 sequestration potential of coastal ocean alkalinization. *Earth's Future*, *5*(12), 1252–1266. Retrieved from https://agupubs.onlinelibrary.wiley.com/doi/abs/10.1002/2017EF000659 doi: https://doi.org/10.1002/2017EF000659

Gurney, G. G., Mangubhai, S., Fox, M., Kiatkoski Kim, M., & Agrawal, A. (2021). Equity in environmental governance: perceived fairness of distributional justice principles in marine co-management. *Environmental Science & Policy*, *124*, 23–32. Retrieved from https://www.sciencedirect.com/science/article/pii/S1462901121001489 doi: https://doi.org/10.1016/j.envsci.2021.05.022

Hartmann, J., Suitner, N., Lim, C., Schneider, J., Marín-Samper, L., Arístegui, J.,

... Riebesell, U. (2023). Stability of alkalinity in ocean alkalinity enhancement (oae) approaches – consequences for durability of co_2 storage. *Biogeosciences*, *20*(4), 781–802. Retrieved from https://bg.copernicus.org/articles/20/781/2023/ doi: 10.5194/bg-20-781-2023

Hartmann, J., West, A. J., Renforth, P., Köhler, P., De La Rocha, C. L., Wolf-Gladrow, D. A., ... Scheffran, J. (2013). Enhanced chemical weathering as a geoengineering strategy to reduce atmospheric carbon dioxide, supply nutrients, and mitigate ocean acidification. *Reviews of Geophysics*, *51*(2), 113–149. Retrieved from https://agupubs.onlinelibrary.wiley.com/doi/abs/10.1002/rog.20004 doi: https://doi.org/10.1002/rog.20004

He, J., & Tyka, M. D. (2023). Limits and co_2 equilibration of near-coast alkalinity enhancement. *Biogeosciences*, *20*(1), 27–43. Retrieved from https://bg.copernicus.org/articles/20/27/2023/ doi: 10.5194/bg-20-27-2023

Ho, D. T. (2023). Carbon dioxide removal is not a current climate solution — we need to change the narrative. *Nature*, *616*, 9. doi: 10.1038/d41586-023-00953-x

IEA. (2022). *Coal 2022* (Tech. Rep.). Retrieved from https://www.iea.org/reports/coal-2022

Ilyina, T., Wolf-Gladrow, D., Munhoven, G., & Heinze, C. (2013). Assessing the potential of calcium-based artificial ocean alkalinization to mitigate rising atmospheric co_2 and ocean acidification. *Geophysical Research Letters*, *40*(22), 5909–5914. Retrieved from https://agupubs.onlinelibrary.wiley.com/doi/abs/10.1002/2013GL057981 doi: https://doi.org/10.1002/2013GL057981

Jayathilake, D. R. M., & Costello, M. J. (2020). A modelled global distribution of the kelp biome. *Biological Conservation*, *252*, 108815. Retrieved from https://www.sciencedirect.com/science/article/pii/S0006320720308739 doi: https://doi.org/10.1016/j.biocon.2020.108815

Keller, D. P., Lenton, A., Scott, V., Vaughan, N. E., Bauer, N., Ji, D., ... Zickfeld, K. (2018). The carbon dioxide removal model intercomparison project (cdr-mip): rationale and experimental protocol for cmip6. *Geoscientific Model Development*, *11*(3), 1133–1160. Retrieved from https://gmd.copernicus.org/articles/11/1133/2018/ doi: 10.5194/gmd-11-1133-2018

Kerr, R. A. (2000). A north atlantic climate pacemaker for the centuries. *Science*, *288*(5473), 1984–1985. Retrieved from https://www.science.org/doi/abs/10.1126/science.288.5473.1984 doi: 10.1126/science.288.5473.1984

Key, R. M., Kozyr, A., Sabine, C. L., Lee, K., Wanninkhof, R., Bullister, J. L., ... Peng, T.-H. (2004). A global ocean carbon climatology: Results from global data analysis project (glodap). *Global Biogeochemical Cycles*, *18*. Retrieved from https://agupubs.onlinelibrary.wiley.com/doi/abs/10.1029/2004GB002247 doi: https://doi.org/10.1029/2004GB002247

Kheshgi, H. S. (1995). Sequestering atmospheric carbon dioxide by increasing ocean alkalinity. *Energy*, *20*(9), 915–922.

Kroeker, K. J., Kordas, R. L., Crim, R., Hendriks, I. E., Ramajo, L., Singh, G. S., ... Gattuso, J.-P. (2013). Impacts of ocean acidification on marine organisms: quantifying sensitivities and interaction with warming. *Global Change Biology*, *19*(6), 1884–1896. Retrieved from https://onlinelibrary.wiley.com/doi/abs/10.1111/gcb.12179 doi: https://doi.org/10.1111/gcb.12179

Kuhlbrodt, T., Jones, C. G., Sellar, A., Storkey, D., Blockley, E., Stringer, M., ... Walton, J. (2018). The low-resolution version of hadgem3 gc3. 1: Development and evaluation for global climate. *Journal of Advances in Modeling Earth Systems*, *10*(11), 2865–2888.

Kwiatkowski, L., Torres, O., Bopp, L., Aumont, O., Chamberlain, M., Christian, J. R., ... Ziehn, T. (2020). Twenty-first century ocean warming, acidification, deoxygenation, and upper-ocean nutrient and primary production

decline from cmip6 model projections. *Biogeosciences*, *17*(13), 3439–3470. Retrieved from https://bg.copernicus.org/articles/17/3439/2020/ doi: 10.5194/bg-17-3439-2020

Köhler, P. (2020). Anthropogenic co_2 of high emission scenario compensated after 3500 years of ocean alkalinization with an annually constant dissolution of 5 pg of olivine. *Frontiers in Climate*, *2*. Retrieved from https://www.frontiersin.org/articles/10.3389/fclim.2020.575744 doi: 10.3389/fclim.2020.575744

Köhler, P., Hartmann, J., & Wolf-Gladrow, D. A. (2010). Geoengineering potential of artificially enhanced silicate weathering of olivine. *Proceedings of the National Academy of Sciences*, *107*(47), 20228-20233. Retrieved from https://www.pnas.org/doi/abs/10.1073/pnas.1000545107 doi: 10.1073/pnas.1000545107

Lampitt, R. S., Achterberg, E. P., Anderson, T. R., Hughes, J. A., Iglesias-Rodriguez, M. D., Kelly-Gerreyn, B. A., ... Yool, A. (2008). Ocean fertilization: a potential means of geoengineering? *Philosophical transactions. Series A, Mathematical, physical, and engineering sciences*, *366*, 3919–3945. doi: 10.1098/rsta.2008.0139

Lan, X., Tans, P., & Thoning, K. (2023, 7). *Trends in globally-averaged co2 determined from noaa global monitoring laboratory measurements, version 2023-07* (Tech. Rep.). Global Monitoring Laboratory, NOAA. doi: 10.15138/9N0H-ZH07

Lenton, T. M. (2010). The potential for land-based biological co_2 removal to lower future atmospheric co_2 concentration. *Carbon Management*, *1*(1), 145–160. Retrieved from https://doi.org/10.4155/cmt.10.12 doi: 10.4155/cmt.10.12

Madec, G., Bourdallé-Badie, R., Bouttier, P.-A., Bricaud, C., Bruciaferri, D., Calvert, D., ... others (2017). Nemo ocean engine [Computer software manual].

Madec, G., Delecluse, P., Imbard, M., & Levy, C. (1997). Ocean general circulation model reference manual [Computer software manual].

Madec, G., & Team, T. N. (2008). NEMO ocean engine, Note du pole de modélisation de l'IPSL n°27 [Computer software manual]. ISSN N°1228-1619.

Mahmoudkhani, M., & Keith, D. W. (2009). Low-energy sodium hydroxide recovery for co_2 capture from atmospheric air—thermodynamic analysis. *International Journal of Greenhouse Gas Control*, *3*(4), 376–384. Retrieved from https://www.sciencedirect.com/science/article/pii/S1750583609000176 doi: https://doi.org/10.1016/j.ijggc.2009.02.003

Moras, C. A., Bach, L. T., Cyronak, T., Joannes-Boyau, R., & Schulz, K. G. (2022). Ocean alkalinity enhancement – avoiding runaway $caco_3$ precipitation during quick and hydrated lime dissolution. *Biogeosciences*, *19*(15), 3537–3557. Retrieved from https://bg.copernicus.org/articles/19/3537/2022/ doi: 10.5194/bg-19-3537-2022

National Geophysical Data Center, N. (1993). *5-minute gridded global relief data (etopo5)* (Tech. Rep.).

O'Neill, B. C., Tebaldi, C., van Vuuren, D. P., Eyring, V., Friedlingstein, P., Hurtt, G., ... Sanderson, B. M. (2016). The scenario model intercomparison project (scenariomip) for cmip6. *Geoscientific Model Development*, *9*(9), 3461–3482. Retrieved from https://gmd.copernicus.org/articles/9/3461/2016/ doi: 10.5194/gmd-9-3461-2016

Oreska, M. P. J., McGlathery, K. J., & Porter, J. H. (2017). Seagrass blue carbon spatial patterns at the meadow-scale. *PLOS ONE*, *12*, 1–18. Retrieved from https://doi.org/10.1371/journal.pone.0176630 doi: 10.1371/journal.pone.0176630

Orr, J. C., & Epitalon, J.-M. (2015). Improved routines to model the ocean carbon-

ate system: mocsy 2.0. *Geoscientific Model Development*, *8*(3), 485–499. Retrieved from https://gmd.copernicus.org/articles/8/485/2015/ doi: 10.5194/gmd-8-485-2015

Pineda, M.-C., Strehlow, B., Sternel, M., Duckworth, A., den Haan, J., Jones, R., & Webster, N. (2017). Effects of sediment smothering on the sponge holobiont with implications for dredging management. *Scientific Reports*, *7*. Retrieved from https://doi.org/10.1038/s41598-017-05243-x doi: 10.1038/s41598-017-05243-x

Planchat, A., Kwiatkowski, L., Bopp, L., Torres, O., Christian, J. R., Butenschön, M., ... Stock, C. (2023). The representation of alkalinity and the carbonate pump from cmip5 to cmip6 earth system models and implications for the carbon cycle. *Biogeosciences*, *20*(7), 1195–1257. Retrieved from https://bg.copernicus.org/articles/20/1195/2023/ doi: 10.5194/bg-20-1195-2023

Popova, E., Vousden, D., Sauer, W. H., Mohammed, E. Y., Allain, V., Downey-Breedt, N., ... Yool, A. (2019). Ecological connectivity between the areas beyond national jurisdiction and coastal waters: Safeguarding interests of coastal communities in developing countries. *Marine Policy*, *104*, 90–102. Retrieved from https://www.sciencedirect.com/science/article/pii/S0308597X19300764 doi: https://doi.org/10.1016/j.marpol.2019.02.050

Power, S., Casey, T., Folland, C., Colman, A., & Mehta, V. (1999). Inter-decadal modulation of the impact of enso on australia. *Climate Dynamics*, *15*. doi: 10.1007/s003820050284

Rae, J. G. L., Hewitt, H. T., Keen, A. B., Ridley, J. K., West, A. E., Harris, C. M., ... Walters, D. N. (2015). Development of the global sea ice 6.0 cice configuration for the met office global coupled model. *Geoscientific Model Development*, *8*(7), 2221–2230.

Raven, J. A., & Falkowski, P. G. (1999). Oceanic sinks for atmospheric co_2. *Plant, Cell & Environment*, *22*(6), 741–755. doi: https://doi.org/10.1046/j.1365-3040.1999.00419.x

Renforth, P. (2012). The potential of enhanced weathering in the uk. *International Journal of Greenhouse Gas Control*, *10*, 229–243. Retrieved from https://www.sciencedirect.com/science/article/pii/S1750583612001466 doi: https://doi.org/10.1016/j.ijggc.2012.06.011

Renforth, P., & Henderson, G. (2017). Assessing ocean alkalinity for carbon sequestration. *Reviews of Geophysics*, *55*(3), 636–674. Retrieved from https://agupubs.onlinelibrary.wiley.com/doi/abs/10.1002/2016RG000533 doi: https://doi.org/10.1002/2016RG000533

Rimstidt, J. D., Brantley, S. L., & Olsen, A. A. (2012). Systematic review of forsterite dissolution rate data. *Geochimica et Cosmochimica Acta*, *99*, 159–178. Retrieved from https://www.sciencedirect.com/science/article/pii/S001670371200525X doi: https://doi.org/10.1016/j.gca.2012.09.019

Robinson, J., New, A. L., Popova, E. E., Srokosz, M. A., & Yool, A. (2017). Far-field connectivity of the uk's four largest marine protected areas: Four of a kind? *Earth's Future*, *5*(5), 475–494. Retrieved from https://agupubs.onlinelibrary.wiley.com/doi/abs/10.1002/2016EF000516 doi: https://doi.org/10.1002/2016EF000516

Rogelj, J., Popp, A., Calvin, K. V., Luderer, G., Emmerling, J., Gernaat, D., ... Tavoni, M. (2018). Scenarios towards limiting global mean temperature increase below 1.5°c. *Nature Climate Change*, *8*, 325–332. doi: 10.1038/s41558-018-0091-3

Sanz-Pérez, E. S., Murdock, C. R., Didas, S. A., & Jones, C. W. (2016). Direct capture of co_2 from ambient air. *Chemical Reviews*, *116*(19), 11840–11876. doi: 10.1021/acs.chemrev.6b00173

Schellnhuber, H. J., Rahmstorf, S., & Winkelmann, R. (2016). Why the right cli-

mate target was agreed in paris. *Nature Climate Change*, *6*, 649–653. doi: 10.1038/nclimate3013

Schuiling, R. D., & Krijgsman, P. (2006). Enhanced weathering: An effective and cheap tool to sequester co_2. *Climatic Change*, *74*, 349–354. doi: 10.1007/s10584-005-3485-y

Séférian, R., Berthet, S., Yool, A., Palmiéri, J., Bopp, L., Tagliabue, A., ... Yamamoto, A. (2020). Tracking improvement in simulated marine biogeochemistry between cmip5 and cmip6. *Current Climate Change Reports*, *6*, 95–119. doi: 10.1007/s40641-020-00160-0

Sellar, A. A., Jones, C. G., Mulcahy, J. P., Tang, Y., Yool, A., Wiltshire, A., ... others (2019). Ukesm1: Description and evaluation of the uk earth system model. *Journal of Advances in Modeling Earth Systems*, *11*(12), 4513–4558.

Shayka, B. F., Hesselbarth, M. H. K., Schill, S. R., Currie, W. S., & Allgeier, J. E. (2023). The natural capital of seagrass beds in the caribbean: evaluating their ecosystem services and blue carbon trade potential. *Biology Letters*, *19*(6), 20230075. Retrieved from `https://royalsocietypublishing.org/doi/abs/10.1098/rsbl.2023.0075` doi: 10.1098/rsbl.2023.0075

Tilmes, S., Mills, M. J., Niemeier, U., Schmidt, H., Robock, A., Kravitz, B., ... English, J. M. (2015). A new geoengineering model intercomparison project (geomip) experiment designed for climate and chemistry models. *Geoscientific Model Development*, *8*(1), 43–49. Retrieved from `https://gmd.copernicus.org/articles/8/43/2015/` doi: 10.5194/gmd-8-43-2015

Tollesfon, J. (2023). Can adding antacids to the ocean slow global warming? *Nature*, *618*, 902–904. doi: 10.1038/d41586-023-02032-7

Tyka, M. D., Van Arsdale, C., & Platt, J. C. (2022). Co_2 capture by pumping surface acidity to the deep ocean. *Energy Environ. Sci.*, *15*, 786–798. Retrieved from `http://dx.doi.org/10.1039/D1EE01532J` doi: 10.1039/D1EE01532J

UNEP-WCMC, & Short, F. (2021). Global distribution of seagrasses (version 7.1). Retrieved from `https://doi.org/10.34892/x6r3-d211`

van Gennip, S. J., Popova, E. E., Yool, A., Pecl, G. T., Hobday, A. J., & Sorte, C. J. B. (2017). Going with the flow: the role of ocean circulation in global marine ecosystems under a changing climate. *Global Change Biology*, *23*(7), 2602–2617. Retrieved from `https://onlinelibrary.wiley.com/doi/abs/10.1111/gcb.13586` doi: https://doi.org/10.1111/gcb.13586

Vesper, D. J., Edenborn, H. M., Billings, A. A., & Moore, J. E. (2015). A field-based method for determination of dissolved inorganic carbon in water based on co_2 and carbonate equilibria. *Water, air, and soil pollution*, *226*. Retrieved from `https://doi.org/10.1007/s11270-015-2348-z` doi: 10.1007/s11270-015-2348-z

Voosen, P. (2022). Ocean geoengineering scheme aces field test. *Science*, *378*, 1266–1267. doi: 10.1126/science.adg3935

Wang, F., & Dreisinger, D. (2022). Carbon mineralization with concurrent critical metal recovery from olivine. *Proceedings of the National Academy of Sciences*, *119*(32), e2203937119. Retrieved from `https://www.pnas.org/doi/abs/10.1073/pnas.2203937119` doi: 10.1073/pnas.2203937119

Williams, K. D., Copsey, D., Blockley, E. W., Bodas-Salcedo, A., Calvert, D., Comer, R., ... Xavier, P. K. (2018). The met office global coupled model 3.0 and 3.1 (gc3.0 and gc3.1) configurations. *Journal of Advances in Modeling Earth Systems*, *10*(2), 357–380.

Williamson, P. (2016). Emissions reduction: Scrutinize co_2 removal methods. *Nature*, *530*, 153–155. doi: 10.1038/530153a

Yool, A., & Palmieri, J. (2023, Jul). *Supporting data for manuscript: "global-scale evaluation of coastal ocean alkalinity enhancement in a fully-coupled earth system model".* Zenodo. doi: 10.5281/zenodo.8193166

Yool, A., Palmiéri, J., Jones, C. G., de Mora, L., Kuhlbrodt, T., Popova, E. E., ...

others (2021). Evaluating the physical and biogeochemical state of the global ocean component of ukesm1 in cmip6 historical simulations. *Geoscientific Model Development*, *14*(6), 3437–3472.

Yool, A., Popova, E. E., & Anderson, T. R. (2013). Medusa-2.0: an intermediate complexity biogeochemical model of the marine carbon cycle for climate change and ocean acidification studies. *Geoscientific Model Development*, *6*(5), 1767–1811.

Yool, A., Shepherd, J. G., Bryden, H. L., & Oschlies, A. (2009). Low efficiency of nutrient translocation for enhancing oceanic uptake of carbon dioxide. *Journal of Geophysical Research: Oceans*, *114*(C8). Retrieved from `https://agupubs.onlinelibrary.wiley.com/doi/abs/10.1029/2008JC004792` doi: https://doi.org/10.1029/2008JC004792

Yu, C., Cheng, J. J., Jones, L. G., Wang, Y. Y., Faillace, E., Loureiro, C., & Chia, Y. P. (1993, 4). *Data collection handbook to support modeling the impacts of radioactive material in soil* (Tech. Rep.). Retrieved from `https://www.osti.gov/biblio/10162250` doi: 10.2172/10162250

Zhang, Y., Wallace, J. M., & Battisti, D. S. (1997). Enso-like interdecadal variability: 1900–93. *Journal of Climate*, *10*(5), 1004–1020. Retrieved from `https://journals.ametsoc.org/view/journals/clim/10/5/1520-0442_1997_010_1004_eliv_2.0.co_2.xml` doi: https://doi.org/10.1175/1520-0442(1997)010⟨1004:ELIV⟩2.0.CO;2

RunID	**Simulation**	**OAE rate**	**OAE depth**	**JobID**
CTRL	control	–	–	u-co094
EXP1	OAE base experiment	×1.0	100 m	u-cp799
EXP2	OAE rate sensitivity 1	×0.5	100 m	u-ct620
EXP3	OAE rate sensitivity 2	×2.0	100 m	u-ct619
EXP4	OAE depth sensitivity 1	×1.0	0 m	u-cp800
EXP5	OAE depth sensitivity 2	×1.0	200 m	u-cn857

Table 1. Experiment summary listing the simulations and RunIDs used in this manuscript, their TA addition rates and maximum depths of alkalinity addition (see main text), and the formal JobIDs used by the UKMO's Rose suite management and MASS archive systems.

Property	Primary		OAE rate		OAE depth	
	CTRL	EXP1	EXP2	EXP3	EXP4	EXP5
	2020s					
OAE addition, Teq y^{-1}	–	26.561	13.422	53.236	26.881	26.718
Surface TA, meq m^{-3}	2320.217	2323.392	2322.230	2326.834	2324.312	2323.336
Δ CTRL, %	–	+0.137%	+0.087%	+0.285%	+0.176%	+0.134%
Surface DIC, mmol m^{-3}	2078.315	2080.386	2079.039	2081.860	2080.345	2079.978
Δ CTRL, %	–	+0.100%	+0.035%	+0.171%	+0.098%	+0.080%
Surface DIC:TA, mol $(eq)^{-1}$	–	0.652	0.360	0.536	0.496	0.533
	2090s					
OAE addition, Teq y^{-1}	–	36.559	18.404	72.698	36.762	36.660
Surface TA, meq m^{-3}	2323.628	2341.345	2331.925	2358.944	2341.785	2340.720
Δ CTRL, %	–	+0.762%	+0.357%	+1.520%	+0.781%	+0.736%
Surface DIC, mmol m^{-3}	2211.549	2225.697	2218.077	2239.911	2225.712	2225.336
Δ CTRL, %	–	+0.640%	+0.295%	+1.282%	+0.640%	+0.623%
Surface DIC:TA, mol $(eq)^{-1}$	–	0.799	0.787	0.803	0.780	0.807
Global TA, Peq	3286.151	3288.481	3287.318	3290.797	3288.483	3288.490
Δ CTRL	–	2.330	1.168	4.646	2.332	2.339
Global DIC, Pmol	3102.093	3103.907	3103.013	3105.661	3104.106	3103.847
Δ CTRL	–	1.814	0.920	3.568	2.013	1.755
Global DIC:TA, mol $(eq)^{-1}$	–	0.779	0.788	0.768	0.863	0.750
Atm. xCO_2, ppm	1118.433	1108.826	1113.285	1097.617	1107.482	1109.679
Δ CTRL	–	-9.607	-5.148	-20.816	-10.951	-8.755
SAT, °C	21.251	21.196	21.251	21.060	21.228	21.197
Δ CTRL	–	-0.055	-0.000	-0.191	-0.023	-0.054
NPP, Pg C y^{-1}	40.095	39.722	39.918	40.048	39.967	40.182
Δ CTRL, %	–	-0.929%	-0.441%	-0.118%	-0.317%	+0.218%
C_{org} export, Pg C y^{-1}	5.042	5.001	5.020	5.058	5.049	5.076
Δ CTRL, %	–	-0.814%	-0.436%	+0.313%	+0.146%	+0.670%
$CaCO_3$ export, Pg C y^{-1}	0.073	0.075	0.074	0.080	0.075	0.077
Δ CTRL, %	–	+2.216%	+1.050%	+8.610%	+2.722%	+4.817%
Surface pH, –	7.667	7.675	7.671	7.683	7.676	7.675
Δ CTRL	–	+0.008	+0.004	+0.016	+0.009	+0.008
Surface $\Omega_{calcite}$, –	2.385	2.444	2.414	2.499	2.450	2.440
Δ CTRL	–	+0.058	+0.028	+0.113	+0.064	+0.055

Table 2. Global means and integrals of key carbon cycle properties across simulations, including changes between experimental and control simulations. Results are shown for the final decade of the experiments (2090s), with a subset given for the first decade of the experiments (2020s). The final portion of the table lists several properties associated with the wider marine biogeochemistry. Changes from the control simulation are listed as either absolute or relative (as a percentage) where appropriate.

Property	**Primary**		**OAE rate**		**OAE depth**	
	CTRL	**EXP1**	**EXP2**	**EXP3**	**EXP4**	**EXP5**
			(a) **All fluxes**			
Global	375.4133	399.5453	387.8226	422.0827	401.6247	398.6026
Shelf	27.6534	40.2355	34.0974	51.5418	41.4630	39.9086
Off-shelf	347.7599	359.3098	353.7252	370.5409	360.1618	358.6940
			(b) **All Δ fluxes**			
Global	–	24.1320	12.4093	46.6694	26.2114	23.1893
Shelf	–	12.5821	6.4440	23.8884	13.8096	12.2552
Off-shelf	–	11.5498	5.9653	22.7810	12.4018	10.9341
			(c) **Positive-only Δ fluxes**			
Global	–	28.4286	16.6112	50.7453	30.5310	27.7695
Shelf	–	12.6808	6.5675	23.9659	13.9009	12.3656
Off-shelf	–	15.7478	10.0437	26.7794	16.6301	15.4038
			(d) **Negative-only Δ fluxes**			
Global	–	-4.2967	-4.2019	-4.0759	-4.3197	-4.5802
Shelf	–	-0.0987	-0.1235	-0.0775	-0.0914	-0.1105
Off-shelf	–	-4.1980	-4.0785	-3.9984	-4.2283	-4.4697

Table 3. Global and regional totals of time-integrated (2020–2100) air-sea CO_2 flux for the CTRL and experiment ensemble. Section (a) lists the CO_2 flux integrated globally, and – using OAE as the delimiting factor – for shelf and off-shelf subregions. Section (b) presents the corresponding difference in CO_2 flux between each member of the experimental ensemble and the CTRL simulation, again globally and for shelf / off-shelf subregions. Sections (c) and (d) present these same differences in CO_2 flux, but integrated solely for positive (ingassing) and negative (outgassing) areas respectively. All fluxes are in Pg C.

RunID	m	C	r^2
EXP1	0.800	-0.037	0.922
EXP2	0.793	-0.003	0.820
EXP3	0.798	-0.104	0.972
EXP4	0.811	0.091	0.913
EXP5	0.799	-0.082	0.934

Table 4. Linear regression of Δ DIC against added Δ TA for each model experiment, using the CTRL simulation to calculate perturbation. Regressions are of the form Δ DIC = $m \times$ Δ TA + C, with the listed coefficient of determination. Regressions use model cells, but these are weighted for cell volume.

Property	**Wor.**	**Atl.**	**Pac.**	**Ind.**	**Sou.**	**Arc.**
OAE addition, %	–	26.9792	47.8014	20.3215	0.7122	3.1912
Inventory Δ TA, %	–	37.9700	21.7656	28.8801	5.3235	5.0914
Inventory Δ DIC, %	–	38.1174	21.0030	28.9847	4.7295	6.0017
Surface Δ TA, meq m^{-3}	17.7243	26.2680	9.3436	39.1122	5.4197	18.1509
Surface Δ DIC, mmol m^{-3}	14.1556	21.7516	6.6861	31.5036	4.0167	18.0115

Table 5. Metrics of key carbon cycle properties from the 2090s for the World, Atlantic, Pacific, Indian, Southern and Arctic oceans. OAE addition is the percentage breakdown of TA addition averaged over the 2090s. Inventories of Δ TA and DIC are the percentage breakdowns of where the total TA added and the extra DIC absorbed is located in the ocean domain in the 2090s. The surface Δ TA and DIC concentrations are the regional means of these quantities for the 2090s.

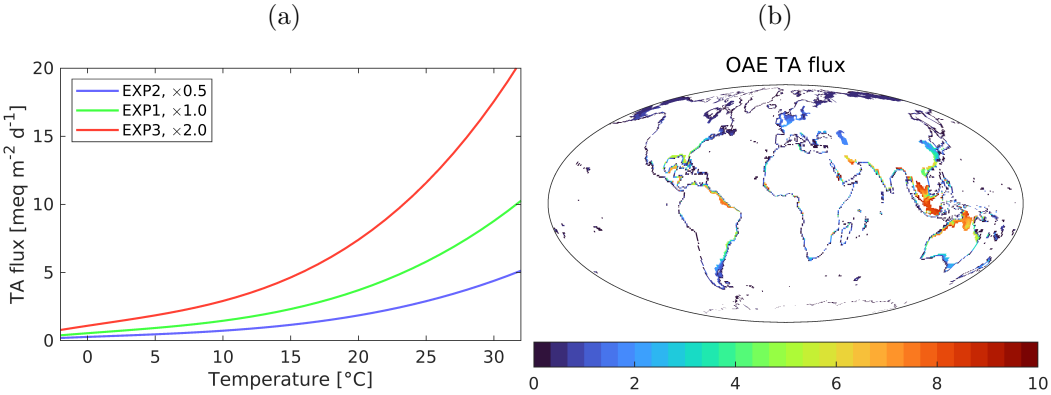

Figure 1. Panels illustrate the TA flux used in the simulated OAE experiments. (a) TA flux as a function of ambient seawater temperature. The green line is the default function used in EXP1. The half and double fluxes used in sensitivity experiments EXP2 and EXP3 are also shown. (b) A geographical map of the TA flux realised in EXP1 for the year 2020 in meq m^{-2} d^{-1}.

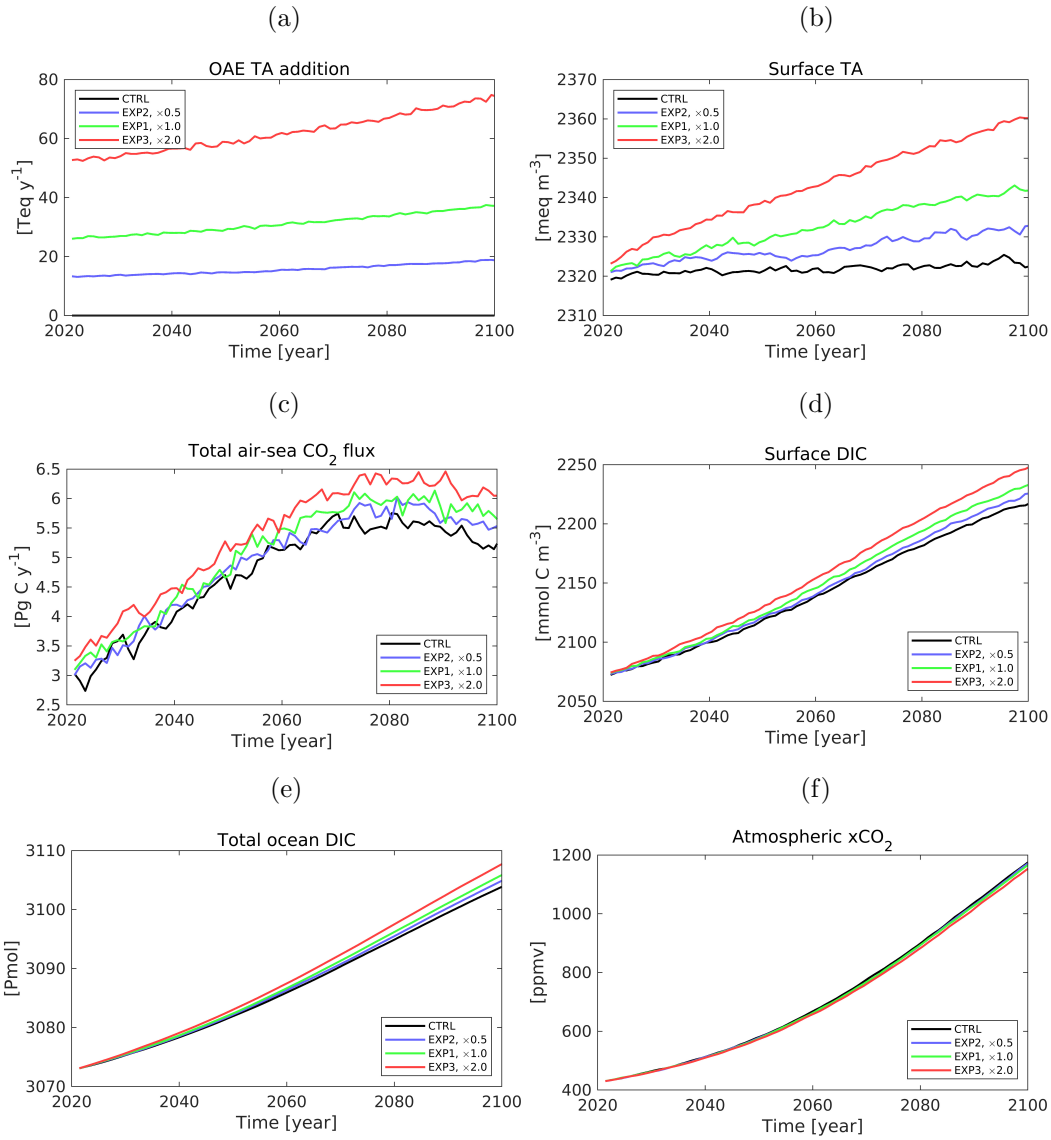

Figure 2. Time series plots of global integrals and averages for the period 2020–2100: (a) global integral of TA added by OAE (Teq y^{-1}); (b) global mean surface TA concentration (meq m^{-3}); (c) global integral of air-sea CO_2 flux (Pg C y^{-1}); (d) global mean surface DIC concentration (mmol C m^{-3}); (e) global integral of DIC (Pmol C); (f) atmospheric CO_2 concentration (ppmv). Panels show CTRL (black), EXP1 (green), EXP2 (blue; ×0.5) and EXP3 (red; ×2.0) simulations.

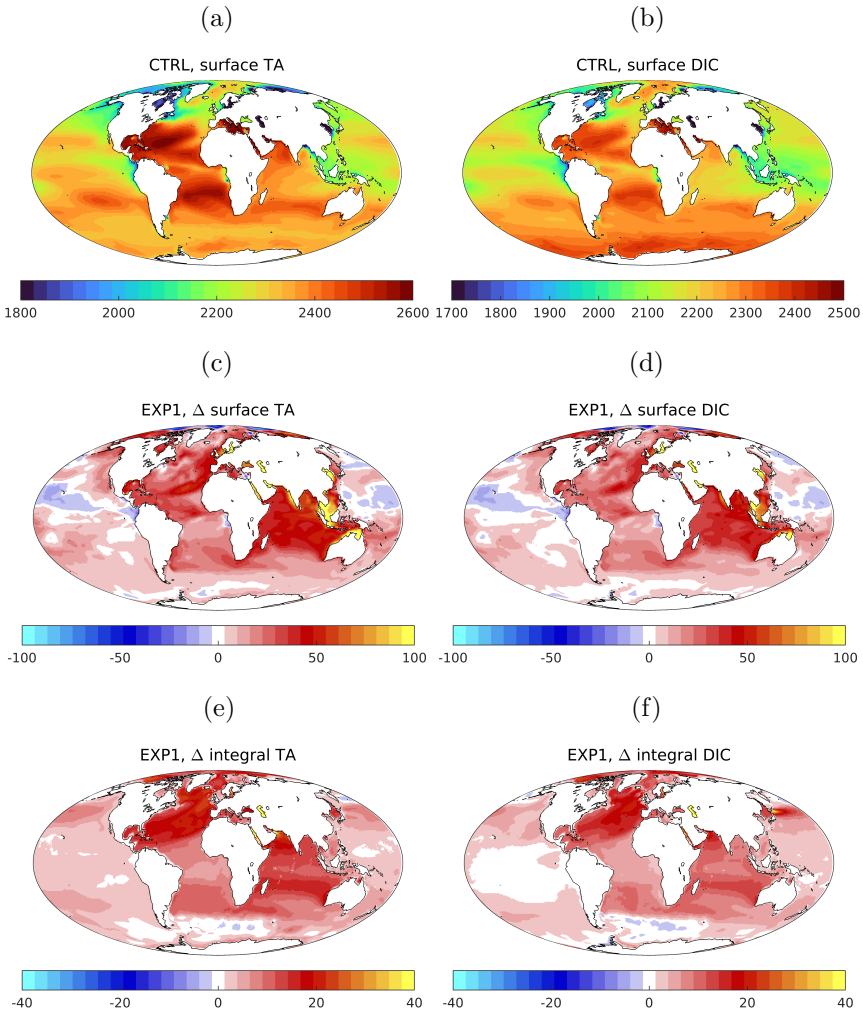

Figure 3. Geographical plots of TA (left column) and DIC (right column) properties, averaged for the 2090s decade: (a) surface TA for the CTRL simulation (meq m^{-3}); (b) surface DIC for the CTRL simulation (mmol C m^{-3}); (c) difference in surface TA, [EXP1 - CTRL] (meq m^{-3}); (d) difference in surface DIC, [EXP1 - CTRL] (mmol C m^{-3}); (e) difference in vertically-integrated TA, [EXP1 - CTRL] (eq m^{-2}); (f) difference in vertically-integrated DIC, [EXP1 - CTRL] (mol C m^{-3}). Note that TA and DIC difference plots share colour axis limits.

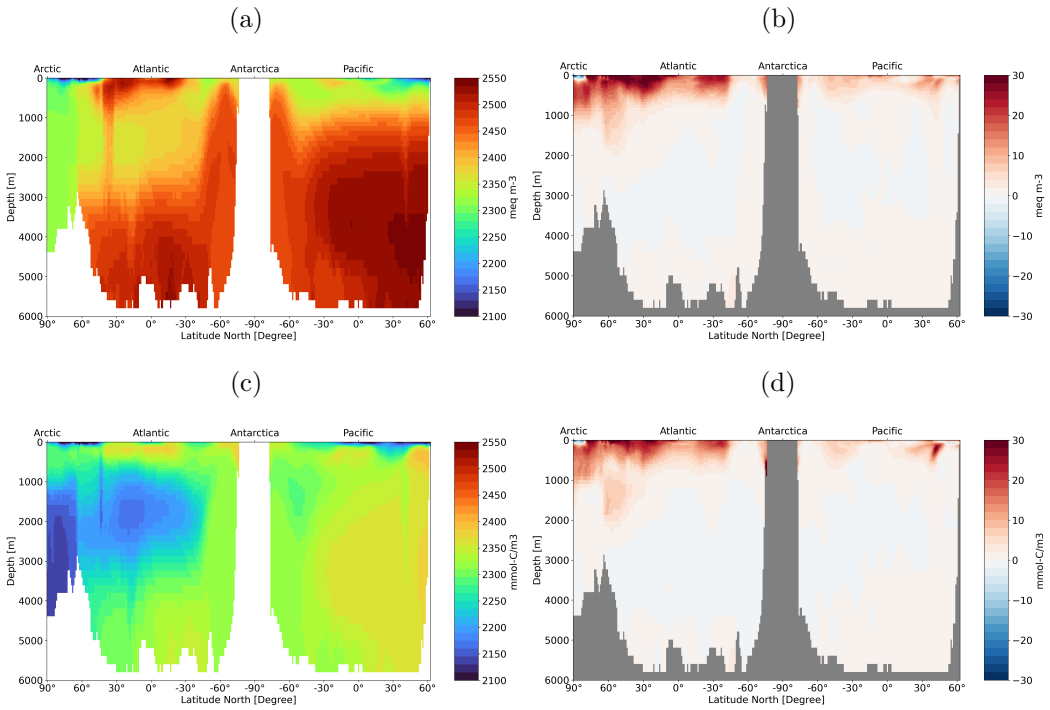

Figure 4. Thermohaline transects showing the patterns of TA and DIC from the Arctic (left), southward through the Atlantic Ocean to the Southern Ocean (centre), then northward through the Pacific Ocean (right). The upper row of plots show (a) section mean TA in the CTRL simulation, and (b) the difference in TA in the EXP1 simulation. The lower row of plots show (c) section mean DIC in the CTRL simulation, and (d) the difference in DIC in the EXP1 simulation. All results are based on the 2090s decadal average. TA in meq m^{-3}, DIC in mmol m^{-3}.

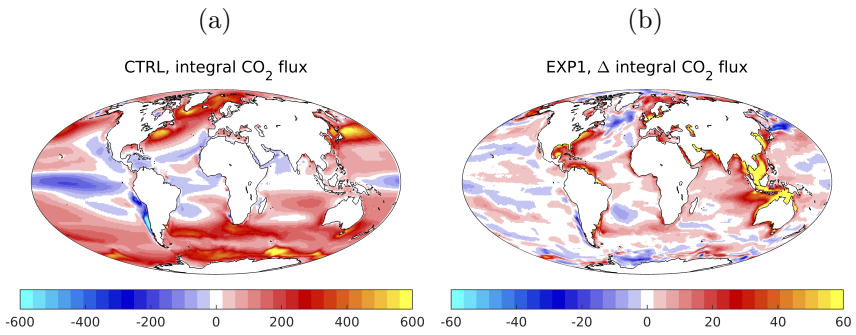

Figure 5. Geographical plots of: (a) time-integrated (2020–2100) CO_2 air-sea flux for the CTRL (mmol C m^{-2}); (b) difference in time-integrated (2020–2100) CO_2 air-sea flux, [EXP1 - CTRL] (mmol C m^{-2}). Note that the scale of panel (b) is 1 order of magnitude than that of panel (a).

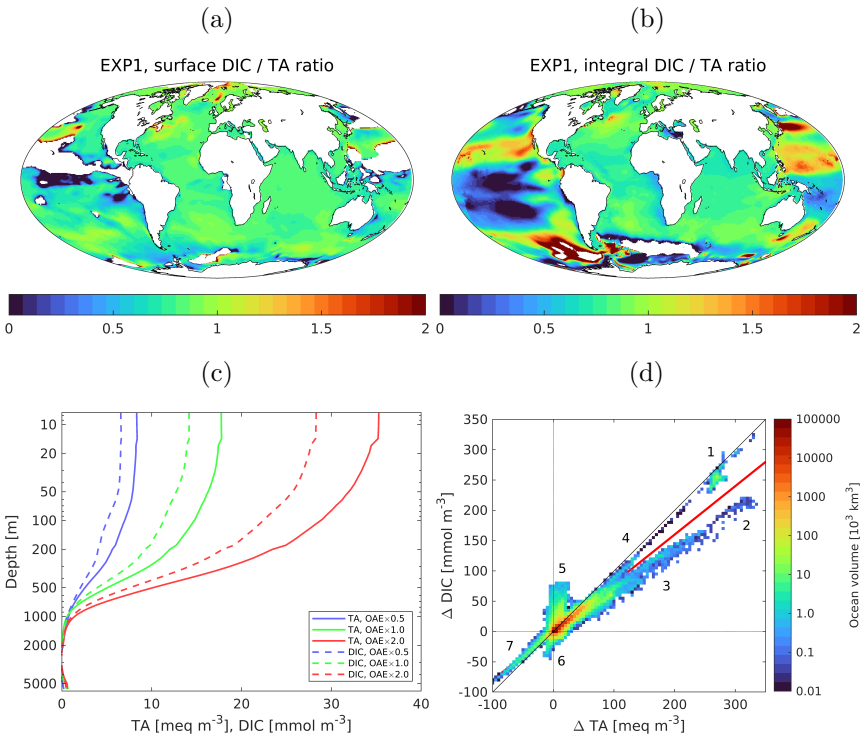

Figure 6. These panels examine the relationship between TA added through OAE and extra DIC absorbed by the simulated ocean. (a) Using surface concentrations from EXP1 shown in figure panels 3c and 3d, the ratio of extra DIC to extra TA (mol C eq^{-1}). (b) Using the vertical integrals from EXP1 in figure panels 3e and 3f, the ratio of extra DIC to extra TA (mol C eq^{-1}). In panels (a) and (b) white ocean regions denote locations where extra TA and/or extra DIC are negative. (c) Global average profiles of extra TA (solid lines) and extra DIC (dashed lines) for EXP1, EXP2 and EXP3. (d) Ocean volume-weighted histogram of extra DIC plotted against extra TA to illustrate the slope of the relationship. The plot's x- and y-axes are consistent, and both the 1:1 (dotted black) and regression (solid red) lines have been added. The numbers shown within the plot identify geographical regions and are discussed in the main text. Note that ocean volume is shown on a logarithmic scale, with blue colours denoting relatively small total volumes. All results are based on the 2090s decadal average.

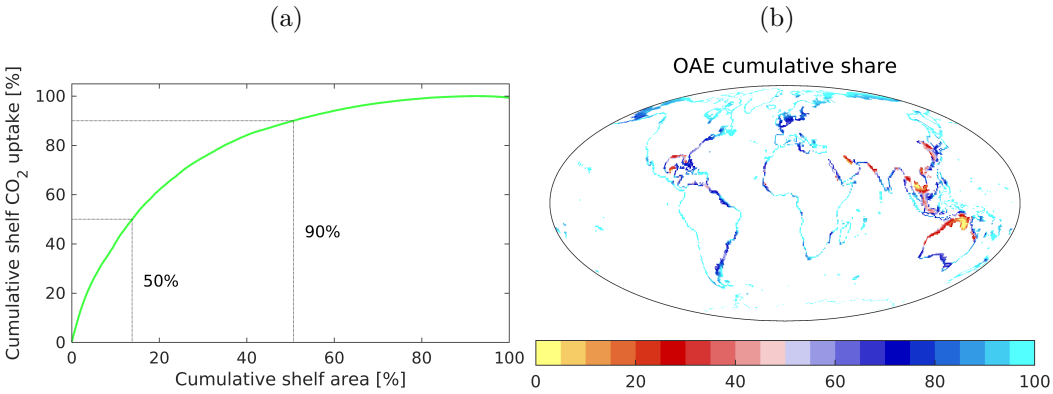

Figure 7. Panels illustrate the large variation in CO_2 uptake between different shelf areas. (a) Model grid cells are sorted by their quantitative contribution to CO_2 uptake, and then the associated shelf area and CO_2 uptake are accumulated. As indicated by the dotted lines, 13.8% of the total shelf area investigated here is responsible for 50% of the CO_2 uptake, and that 50.7% is responsible for 90% of this uptake. (b) To illustrate the geographical distribution of higher efficiency shelf areas, model grid cells are again sorted by their quantitative contribution to extra CO_2 uptake, and then coloured to indicate the percentage of the accumulated CO_2 flux. The colour scale has been chosen such that areas responsible for the first 50% of extra CO_2 uptake are in red colours, while those responsible for the second 50% are in blue. In both panels, the results shown are drawn from EXP1 and averaged over the full simulation period (2020–2100). Note that, because of difficulties in attributing CO_2 uptake to TA releases, both panels only consider CO_2 that is absorbed in the coastal areas where OAE is simulated, while almost 50% of the extra CO_2 uptake in this simulation actually occurs away from these regions.